Cryogenic Electron Tomography Redefines Herpesvirus Capsid Assembly Intermediates Inside the Cell Nucleus.

Stefan L. Oliver[1*], Muyuan Chen[1], Leeya Engel[2], Corey W. Hecksel[1,6], Xueting Zhou[1,7], Michael F. Schmid[1], Ann M. Arvin[4,5], and Wah Chiu[1,3,5].

[1]Division of Cryo-EM and Bioimaging SSRL, SLAC National Accelerator Laboratory, Menlo Park, CA, 94025, USA. [2]Technion Israel Institute of Technology, Haifa, Israel. Departments of [4]Bioengineering, [5]Pediatrics, and [6]Microbiology and Immunology, Stanford University School of Medicine, Stanford, CA, 94305, USA.

[*]Corresponding author: sloliver@stanford.edu

Present addresses:

[6]Merck Research Laboratories, Merck and Co., Rahway, NJ 07033, USA.

[7]Verna and Marrs McLean Department of Biochemistry and Molecular Pharmacology, Baylor College of Medicine, Houston, TX 77030, USA.

Running Title: Cryo-FIB/Cryo-ET of VZV particles.

Key words: Herpesvirus; Varicella-Zoster Virus; capsid; cryo-FIB; cryo-ET; capsid vertex specific component.

Summary.

Herpesviruses encapsulate their double-stranded DNA (dsDNA) genomes within an icosahedral nucleocapsid formed in the infected cell nucleus. Four biochemically purified nucleocapsids have been characterized, but their roles in herpesvirus replication remain controversial. The status of the capsid vertex-specific component (CVSC), essential for capsid stability and dsDNA packaging and retention, is also unclear. By integrating cryogenic focused ion beam milling with electron tomography and subtomogram averaging, we derived atomic models for all protein components, including the CVSC, across different herpesvirus capsid types within infected cell nuclei. Focused classification of pentonal vertex densities revealed differences in CVSC occupancy between genome-filled capsids and capsids lacking dsDNA, highlighting structural heterogeneity and providing insight into distinct capsid assembly stages *in situ*. These intra-nuclear findings redefine the maturation model of herpesvirus capsid assembly, advancing the understanding of herpesvirus replication, and demonstrate the effectiveness of *in situ* electron imaging by studying virus assembly within host cells.

41 **Introduction.**

42 The *Herpesviridae* encompass a large family of viruses comprised of alpha-, beta- and gamma
43 subgenera that infect humans and most animal species with wide ranging health and economic
44 consequences [1-8]. Varicella-zoster virus (VZV), a human alphaherpesvirus, causes varicella
45 (chicken pox) as the primary infection, and zoster (shingles) after reactivation from latency in
46 sensory ganglia[1], and can be life threatening in immunocompromised patients [9-15]. VZV vaccines
47 have reduced morbidity substantially [16-18] and antiviral drugs are effective but neither prevent VZV
48 latency in sensory neurons [19,20] or post-herpetic neuralgia after zoster [21,22], and antiviral resistance
49 can emerge [23,24]. The other two human alphaherpesviruses, herpes simplex virus (HSV) 1 and 2
50 (HSV-2), also create a significant disease burden [25,26]. HSV vaccines are not available and HSV
51 persists in neurons despite antiviral treatment [8]. Vulnerable populations need new interventions
52 for these viruses and against the betaherpesvirus, human cytomegalovirus [4], and the Epstein-Barr
53 and Kaposi's sarcoma gammaherpesviruses, which cause a range of cancers [2,3].

54 Herpesviruses are classified by their distinct 4-layer morphology composed of a double stranded
55 DNA (dsDNA) core, capsid, tegument, and envelope [27]. These complex entities form through a
56 convoluted morphogenesis process starting inside the infected cell nucleus. The dsDNA genome
57 is packaged into newly synthesized capsids that exit the nucleus across nuclear membranes into
58 the cytoplasm, where they traffic to sites of secondary envelopment, completing acquisition of
59 tegument proteins and the lipid envelope containing virus glycoproteins. The nascent enveloped
60 particles are transported in vesicular structures to the plasma membrane and released into the
61 extracellular milieu. The glycoproteins protruding from the lipid membrane then mediate virus
62 entry into neighboring cells and tegument proteins support the intracellular transport of capsids to
63 nuclear pores where the dsDNA genome is injected; additional tegument proteins undergo nuclear
64 translocation to initiate transcription factor functions. Since the herpesvirus capsid structure is
65 essential for virus genome preservation during infection, high-resolution information about the
66 progression of capsid assembly holds great potential to identify novel targets for next generation
67 pharmaceutical interventions and vaccines.

68 Herpesvirus capsids are ~125nm in diameter and share a common icosahedral symmetry with a
69 T=16 geometry made up of 60 asymmetric units. The capsid assembles in the nucleus from 161
70 capsomeres, composed of 150 hexons and 11 pentons that form an icosahedron with 12 vertices,

71 including a unique portal vertex for the packaging of the dsDNA genome and its release through
72 the host cell nuclear pore in newly infected cells. Capsids undergo several transformative stages
73 starting with immature pro-capsids, which are thought to form as capsomeres assemble onto a
74 protein scaffold [28,29]. Maturation of pro-capsids occurs as the scaffold protein is proteolytically
75 digested by its companion protease, triggering a conformational change from a more spherical
76 shape to their final icosahedral morphology, with 20 flat triangular faces and 30 edges. Mature
77 capsids have been conventionally classified as A-, B-, and C-capsids, as they differ in their buoyant
78 densities and morphologies by thin section electron microscopy (EM) [30]. The cavities of C-capsids
79 contain packaged dsDNA genomes, whereas B-capsids have persistent scaffold protein and its
80 associated protease, and A-capsids are described as empty. While A- and B-capsids have been
81 presumed to be dead-end assembly products [29], an alternative hypothesis is that one or both might
82 represent assembly intermediates with the potential to encapsidate dsDNA genomes [31]. Capsid
83 purification can induce artefacts, such as loss of genomic DNA by disruption of the portal vertex
84 cap, creating empty A-capsids from C-capsids [32]. B-capsids accumulated when unit length genome
85 formation was blocked by drug inhibition of the genome-transferase complex [31], suggesting that
86 scaffold protein removal is linked to dsDNA insertion, and capsids with scaffold protein in the
87 cavity might be capsid intermediates rather than representing a failure of genome encapsidation.

88 The proteins that assemble to create a mature herpesvirus capsid have orthologues in all
89 *Herpesviridae*. These include the major capsid protein (MCP), the small capsomere interacting
90 protein (SCP), and the capsid triplex proteins 1 (TRX1) and 2 (TRX2). The multimeric subunits
91 formed by these proteins to produce fully mature capsids have been described at near atomic
92 resolution for all three subgenera of herpesviruses [33-43]. Briefly, the MCP forms the capsomeres
93 of hexons and pentons of the icosahedral capsid. Six copies of the SCP decorate the tops of the
94 hexons. Heterotrimeric triplexes (TRX1 monomer and TRX2 dimer) occupy the canyons between
95 the capsomere towers and cover up the holes in the MCP floor to stabilize the capsid for dsDNA
96 genome containment [33,44]. At each of the 12 capsid vertices, five copies of the capsid vertex
97 specific component (CVSC) bind to triplexes adjacent to the pentons and the unique portal vertex
98 [33]. In HSV, the CVSC is a heteropentamer composed of orthologues shared with VZV; the capsid
99 vertex-specific component 1 (CVC1) monomer, two copies of CVC2, and two copies of the protein
100 designated VP1/2. CVSC binding has been associated with reinforcing capsid stability to
101 withstand the very high packaging pressure of the dsDNA genome [45-47]. At the portal vertex, a

102 dodecamer (VZV ORF54; HSV-1 pUL6), replaces a penton with a portal and tentacle-like helices
103 that ring the DNA translocation channel, and an ATP-driven terminase is recruited to cleave the
104 herpesvirus dsDNA genome for packaging [29,34-36,38,45,48-50]. The CVSC is expected to form part of
105 the portal cap that retains the dsDNA genome in the capsid [29,34-36,38,45,48-50]. The CVSC
106 heteropentamer has also been called the capsid-associated tegument complex because its subunits
107 include the large tegument protein (VP1/2), VZV ORF22 and HSV pUL36 [51]; in HSV and PRV,
108 these orthologues have been identified as inner tegument proteins that function in microtubule-
109 mediated capsid transport to cell nuclei [52,53]. The CVSC of CMV, a betaherpesvirus, has a non-
110 conserved tegument subunit, pp150 [42,54], while gammaherpesvirus CVSCs are thought to resemble
111 those of the alphaherpesviruses [51].

112 Although capsid structures of most human herpesviruses have been solved to better than 4Å
113 resolution by single particle cryo-EM [33,35-41,47], knowledge about capsid assembly as it occurs *in*
114 *situ* within the infected cell nucleus is limited. The CVSC has been proposed to associate with the
115 capsid inside the infected cell nucleus, but the structural organizations of their individual
116 components have not been visualized directly in the nucleus of herpesvirus infected cells [55,56].
117 Whether the assembly of the VP1/2 subunit of the CVSC takes place in the nucleus or cytoplasm
118 is unclear [55,57,58]. Furthermore, despite previous high-resolution structures for VZV capsids, the
119 CVSC and the portal vertex were not resolved in these studies [39,41]. To better understand capsid
120 assembly and the relationship between capsids conventionally classified as A- and B-capsid types
121 compared to the dsDNA containing C-capsids, we sought subnanometer resolution imaging of
122 capsids within VZV infected cells. Imaging inside mammalian cells is challenging because cell
123 thickness limits the penetration of the electron beam and reduces the image contrast due to inelastic
124 scattering and multiple electron scattering [59]. Even at high voltages (1MV) the electron beam can
125 only penetrate 1μm; the nuclei of typical mammalian cells range in size from 5 to 10μm. To
126 overcome this limitation, recent advances in cryogenic focused ion beam and scanning electron
127 microscopy (cryo-FIB/SEM) have been introduced to mill away most of the thick and vitrified
128 cell, leaving a thin lamella of 100 to 400 nm in thickness. When integrated with cryogenic electron
129 tomography (cryo-ET) using a 300 keV electron microscope, 3D volumes are produced at near-
130 atomic resolution by imaging at different tilted angles enabling cryo-tomographic reconstruction
131 [60]. We applied this approach to visualize VZV particles within infected cells in a frozen, hydrated

132 state, without the use of contrast agents, and determined the structures of their component proteins
133 through subtomogram averaging (STA) and computational analyses.

134 Our findings reveal that the CVSC heteropentamer assembles on capsids in the nucleus of infected
135 cells and that the definition of the asymmetric unit of the icosahedral VZV capsid should be
136 expanded to incorporate proteins of the CVSC, which were absent from previous capsid models.
137 Focused classification, including of the unique portal vertex, indicates that genome-filled C-
138 capsids have full CVSC occupancy, defined as the maximum of five heteropentamers. Among
139 capsids lacking dsDNA, empty A-capsids were not detected within the infected cell nucleus
140 whereas capsid assembly intermediates (CAIs) could be distinguished by differences in the number
141 of CVSCs found at the vertices of the icosahedron, which correlated with levels of scaffold protein
142 in the capsid cavity, suggesting a continuum along the maturation pathway. Notably, CAIs would
143 be grouped together as B-capsids based on scaffold protein alone. These observations provide
144 evidence that CVSC acquisition can serve as a temporal marker for the progression of intra-nuclear
145 herpesvirus capsid assembly *in situ*, consistent with its biological importance for ensuring the
146 stability of genome-containing capsids during nuclear egress and formation of complete virus
147 particles in the cytoplasm.

148 **Results.**

149 **VZV morphogenesis visualized within infected cells *in situ* by cryo-FIB-SEM and cryo-ET.**

150 To visualize herpesvirus morphogenesis in 3D-space, a workflow was developed to distribute VZV
151 infected cells evenly on EM grids suitable for cryo-FIB milling. First, because VZV does not yield
152 high titer cell-free virus particles, it was critical to optimize the passage of infected cells onto
153 uninfected cells to initiate infection prior to vitrification. Infection was monitored by the
154 fluorescence RFP signal produced by MeWo cells infected with a recombinant VZV (pOka-TK-
155 RFP) expressing TK-RFP (**Fig. 1**). Second, to overcome the propensity of VZV infected cells to
156 adhere to the grid bars when seeded on SiO_2 EM grids, islands of extracellular matrix were
157 micropatterned within the grid squares (**Fig. 1B**). With this technique, infected cells were
158 positioned centrally within the grid squares after vitrification and ideal for cryo-FIB milling to
159 produce lamella suitable for cryo-ET (**Fig. 1C and 1D**). Tomograms of cryo-FIB milled cells
160 revealed the complex cellular environment in VZV infected cells (**Fig. 1E; Suppl. Fig. 1 to 7;**
161 **Suppl. Table 1 and 2**). Cellular features were readily visible in medium magnification (16.9 to

162 39.1Å/pixel) montage maps used to facilitate cryo-ET tilt series data collection from cells thinned
163 to a target thickness of ~175nm; the nuclear envelope with visible nuclear pores demarcated the
164 intranuclear and cytoplasmic compartments (**Suppl. Fig. 1A, 4A to 7A**). A plethora of vesicular
165 structures, mitochondria, and, within infected cells, VZV capsids and complete virus particles, was
166 visible, facilitating the localization of regions of interest in a tilt series collection. The higher
167 resolution tomographic reconstructions yielded substantial contrast enabling machine learning-
168 based segmentation to identify ribosomes, microtubules, microfilaments, complex vesicular
169 structures, and assembled capsids in the nucleus and sites of virus particle morphogenesis in the
170 cytoplasm (**Suppl. Fig. 7C**).

171 Several critical steps in the herpesvirus replication cycle were captured within cryo-ET tomograms
172 generated from cryo-FIB milled cells infected with VZV (**Fig. 1E; Suppl. Fig. 1 to 8; Suppl.**
173 **Movie 1 to 6**). These included capsids docked at the nuclear pore (**Fig 1Ei; Suppl. Fig 1; Suppl.**
174 **Movie 1**), newly synthesized capsids in the nucleus **Fig 1Eii; Suppl. Fig 3; Suppl. Movie 2**),
175 nuclear egress (**Fig 1Eiii; Suppl. Fig 4; Suppl. Movie 3**), secondary envelopment (**Fig 1Eiv;**
176 **Suppl. Fig 5; Suppl. Movie 4**), VZV particle morphogenesis (**Fig 1Ev; Suppl. Fig. 6 and 7;**
177 **Suppl. Movie 5**), and VZV particles bound to the extracellular plasma membrane surface (**Fig**
178 **1Evi; Suppl. Fig 8; Suppl. Movie 4**), a typical feature of this cell associated virus. Within the
179 infected cell nucleus, pro-capsids and A-, B-, and C-capsids based on conventional morphological
180 features, were distinguishable in 3D-space at this resolution. Procapsids were spherical and
181 contained a solid density of scaffold protein; capsids apparently devoid of scaffold protein or
182 dsDNA (conventional A-capsids) were identified; B-capsids were observed and defined by the
183 presence of scaffold protein (**Fig. 1Eii**); and C-capsids were distinguishable by their cavities filled
184 with dsDNA (**Fig. 1Eiii, 2A and 2B; Suppl. Fig. 4 to 6**). Procapsid assembly precursors were
185 identified within infected cell nuclei, appearing as angular segments of capsomeres associated with
186 scaffold protein with a curvature similar to the procapsids (**Suppl. Fig. 2**). Importantly, high-
187 resolution detail was evident by the visualization of individual capsid capsomeres (**Fig 1Eii,**
188 **Suppl. Fig 3; Suppl. Movie 2**), individual nuclear egress complexes (**Fig 1Eiii, Suppl. Fig 4;**
189 **Suppl. Movie 3**), and individual glycoproteins on enveloped VZV particles in the cytoplasm or
190 bound to the plasma membrane (**Fig. 1Eiv and vi; Suppl. Fig. 5 and 8; Suppl. Movie 5 and 6**).
191 Partially assembled virus particles were observed within cytoplasmic sites of VZV secondary
192 envelopment and morphogenesis, including sites of tegument protein accumulation, based on the

193 electron dense protein surrounding the capsids within the reconstructed tomograms (**Fig. 1Eiv and**
194 **1Ev; Suppl. Fig. 5 and 6**). For example, a VZV light particle, a glycoprotein-studded envelope
195 containing tegument proteins but without a capsid, and a complete particle were observed in a
196 vesicular structure, and in a neighboring vesicular structure, an elongated VZV particle contained
197 a C-capsid and the accumulation of tegument protein associated with a membranous structure
198 (**Suppl. Fig. 7B**). The virus envelope within these vesicular structures was detected by the
199 machine learning-based segmentation (**Suppl. Fig. 7C**). Collectively, these direct visualizations
200 reveal details of the VZV replication cycle previously unobserved in its native hydrated state inside
201 infected cells, particularly for nuclear egress, tegument acquisition during secondary envelopment,
202 and virus glycoprotein interactions with both intra- and extracellular membranes.

203 **Subnanometer reconstruction of VZV capsid proteins in infected cells.**

204 From 194 tilt series, 1,084 capsids were identified and classified based on classical morphological
205 features, the presence or absence of scaffold protein or the virus genome in the capsid cavity. A
206 visual inspection of the image contrast in the capsid cavity revealed a continuum of sparse density,
207 likely scaffolding, suggesting that completely empty A-capsids are absent or very rare within
208 infected cell nuclei (**Suppl. Fig. 9**). Residual scaffold protein was limited enough in some capsids
209 to be obscured by conventional EM techniques due to the plane of the cut in ultrathin sections.
210 The cellular distribution of the 1,084 VZV capsids was primarily localized inside the nucleus
211 (n=980) with only 9.3% detected in the cytoplasm either as naked capsids, without tegument or
212 envelope proteins (n=42), or as complete enveloped VZV particles (n=59) (**Suppl. Table 3**). The
213 capsid distribution was typical for peak particle synthesis of VZV infected cells, which aligns with
214 thymidine kinase (TK) expression, an early gene, as determined by the red fluorescence signal
215 produced from the recombinant pOka-TK-RFP virus.

216 An initial 13Å cryo-ET map of the VZV capsid was generated by subtomogram averaging (STA)
217 of 317 capsids (**Fig. 2; Suppl. Fig. 10**), containing variable quantities of scaffold protein or
218 packaged DNA. This icosahedral symmetry-imposed map clearly shows the T=16 icosahedron,
219 composed of 60 asymmetric units. Each asymmetric unit consists of a single pentonal MCP
220 subunit (P^P), one peripentonal hexon (P), one central hexon (C), and half of an edge hexon (E),
221 along with interdigitating triplexes (Ta, Tb, Tc, Td, and Te) (**Fig. 3C and 3D**). Cryo-ET maps
222 were produced for the vertex around the 5-fold axis (8.3Å) and the 3-fold symmetry axis (8.4Å)

223 by subsequent symmetry expansion and focused refinement of the 317 capsids. (**Fig. 2E and 2F;**
224 **Suppl. Fig. 10**). The 8.3Å vertex map had sufficient resolution to perform segmentation of
225 individual proteins for the pentonal MCP (P^{P}), six MCPs (P^{1-6}) for the peripentonal hexon and the
226 associated small capsomere interacting protein (SCP), triplex proteins TRX1 (monomer) and
227 TRX2 (dimer) that form the $\alpha_2\beta$ heterotrimers of Ta and Tc, and the three proteins, CVC1 (ORF43
228 monomer), CVC2 (ORF34 dimer), and ORF22 dimer, that assemble to form the capsid vertex
229 specific component (CVSC) heteropentamer (**Fig. 3 and 4,; Suppl. Table 4**). Similar to the vertex
230 map, individual proteins were segmented for the 8.4Å 3-fold symmetry axis cryo-ET map for the
231 six MCPs (C^{1-6}) for the central hexon and associated SCP in addition to the TRX1 and TRX2
232 proteins of the Te triplex (**Suppl. Fig. 11**). The densities in both 3- and 5-fold axes of symmetry
233 were segmented using the structure derived from single particle cryo-EM of VZV capsids
234 (7BW6)[39]. All of the features for the pentonal, peripentonal hexon, and central hexon MCPs were
235 apparent, including the tower, consisting of the crown and buttress regions (**Fig. 3A to C; Suppl.**
236 **Fig. 11**), and the HK97 phage capsid protein-like fold facing the interior chamber of the capsid
237 (**Fig. 3D**), which is evolutionary conserved for herpesviruses and dsDNA bacteriophages [61]. The
238 resolution of these regions in the cryo-ET map was supported by the ability to observe densities
239 for alpha helices in each of the MCP, TRX1 and TRX2 proteins and corresponding Map-Q scores
240 (**Fig. 3C; Suppl. Fig. 11C and E; Suppl. Fig. 12; Suppl. Movie 7**). The classical HK97 phage
241 capsid protein fold of the MCP was distinguishable with the long alpha helix (helix 4)
242 interdigitating at the pseudo 3-fold axis of symmetry between the penton and neighboring
243 peripentonal hexon MCPs (**Fig. 3D**). These subnanometer resolution structural details of the MCP,
244 SCP, TRX1 and TRX2 are the first to be visualized inside the nucleus of a herpesvirus-infected
245 cell.

246 **The CVSC heteropentamer assembles as part of the capsid asymmetric unit in infected cell**
247 **nuclei.**

248 The CVSC status as a capsid component has been difficult to assess due to its propensity to
249 disassociate from vertices during herpesvirus capsid purification, including VZV [45,62,39,41]. In
250 contrast, the CVSC density was apparent at all 12 vertices of the capsid structure in infected cell
251 nuclei (**Fig. 2C**). Furthermore, the 8.3Å cryo-ET map of the VZV capsid vertex was of sufficient
252 resolution to extract densities for the CVSC, demonstrating that the heteropentamer is a capsid
253 component acquired independently of the full tegument layer of the virus particle (**Figs. 2E, 4A**

254 **and 4C**). An AlphaFold model of the CVSC structure oriented the head group for each CVC2
255 (ORF34) molecule at a downward angle compared to the extracted CVSC cryo-ET map density
256 (**Suppl. Fig. 13A and 13B**). The CVC2 head group AlphaFold models were fitted into the cryo-
257 EM density with the aid of molecular dynamics flexible fitting (**Suppl. Fig. 13C; Suppl. Movie**
258 **8**), enabling segmentation of the cryo-EM density into the five individual subunits of the CVSC
259 heteropentamer (**Fig. 4A to 4C**). This revealed that the CVC1 subunit (ORF43 monomer), which
260 has a limited interaction with TRX1 from triplex Te, primarily associates with all three Ta triplex
261 subunits along with MCP P^1 and P^2 of the peripentonal hexon from the neighboring asymmetric
262 unit (**Fig. 4B, 4D and 4E**). A helical bundle forms between the CVC1 subunit, the two ORF22
263 proteins and the two CVC2 proteins, enabling the CVC2 head group to interact with the
264 peripentonal hexon facing side of the pentonal MCP crown (**Fig. 4A**). Since almost all capsids
265 analyzed were intra-nuclear, these observations definitively demonstrate that CVSC assembly at
266 the capsid vertices occurs inside the nucleus. Furthermore, these findings enabled us to redefine
267 the asymmetric unit of the mature C-capsid to be composed of six C hexon subunits (MCP and
268 SCP), three E hexon subunits, two and four peripentonal hexon subunits, one pentonal MCP, five
269 interdigitating triplexes, and a single CVSC heteropentamer (**Fig. 2D and 4B**).

270 **CVSC acquisition redefines capsid assembly intermediates formed during herpesvirus**
271 **capsid assembly.**

272 Given uncertainties about the stages of capsid assembly based on studies of purified capsids [45,62,63]
273 [31,64], we investigated the distribution of CVSC heteropentamers at vertices of capsids in infected
274 cells to determine whether the CVSC occupancy could be used to differentiate capsid types and
275 achieve a more precise characterization for the stages of capsid assembly (**Fig. 5**). Uniform
276 Manifold Approximation and Project (UMAP) is a dimension reduction technique that can be used
277 for the visualization and categorization of complex data [65], including structural heterogeneity in
278 single particle Cryo-EM [66,67]. Application of this unsupervised computational approach (**Fig. 5A**)
279 using three-axis orthogonal projection in latent space classified the 317 capsids that were used to
280 generate the 8.3Å vertex cryo-ET map (**Fig. 2**). Each capsid image was aligned to its symmetry
281 axes, and icosahedral symmetry was applied to individual particles before the projections were
282 generated to compensate for the missing wedge effect intrinsic to cryo-ET data [68]. Three clusters
283 were differentiated in latent space, revealing limited versus (i) extensive (ii) scaffold protein in
284 the capsid cavity, and those with packaged DNA (iii) corresponding to C-capsids, as viewed along

285 the 2-, 3-, and 5-fold axes of symmetry and the STA for each class (**Fig. 5A to 5C**). The detection
286 of limited quantities of scaffold protein for class i capsids enabled the differentiation from
287 conventionally designated B-capsids. The absence of any density inside the capsid cavity,
288 previously established for classical empty A-capsids based on conventional negative stained
289 images [30], was not detected within infected cell nuclei. Residual scaffold protein was visible in
290 the native structures preserved by vitrification performed in this study (**Suppl. Fig. 9**). In addition
291 to capsid cavity content differences, the three UMAP capsid clusters were found to differ in CVSC
292 occupancy at the vertices (**Fig. 5D and 5E**). For each of the 317 capsids, sub-particles were
293 extracted from the 12 vertices and aligned to the same C5 symmetry axis. These particles were
294 initially subject to binary reference free focused classification, resulting in two classes reflecting
295 vertices without or with CVSC occupancy (**Fig. 5D and 5E**). The CVSC was either absent or
296 present, with the arms and lobes of the CVSC clearly visible in the C5 symmetry STA maps (**Fig.
297 5D**). Capsid vertices were then classified into those without and with the CVSC and by their
298 UMAP cluster, i to iii (**Fig. 5E**). As expected, CVSC occupancy was highest on C-capsids in
299 infected cells, as has been reported for purified capsids [33,37,40,42,47], and because they are considered
300 complete and ready for egress from the nucleus for final tegumentation and envelopment in the
301 cytoplasm [45]. Persistent scaffold protein is the conventional marker for B-capsids by EM, resulting
302 in greater buoyant density than empty A-capsids [30]. Notably, capsids differed in CVSC occupancy
303 depending on whether scaffold protein was limited or extensive within the capsid cavity, with the
304 former having greater CVSC occupancy than the latter (**Fig. 5B to 5F**). Critically, for the 12
305 vertices of individual capsids, CVSC occupancy at each vertex increased with decreasing levels of
306 scaffold protein density (**Fig. 5F**). Since C-capsids have the highest CVSC occupancy, these
307 findings indicate that capsids with relatively more CVSC occupancy and less scaffold protein are
308 capsid assembly intermediates (CAIs) further along the pathway of capsid maturation than those
309 with less CVSC occupancy and more residual scaffold protein.

310 To further scrutinize the CVSC on capsids in infected cells, vertex particles were subjected to C5
311 symmetry expansion, generating five sub-particles for the asymmetric orientations. Additional
312 focused classification using a mask covering a single CVSC site produced two classes of CVSC
313 occupancy at each individual location, those with or without the heteropentamer. This procedure
314 established the frequency of CVSC heteropentamers, producing vertex sub-particles with either
315 zero copies, 1 to 5 copies, or 2 and 3 copies of non-consecutive CVSC distribution, which were

316 used for STA without symmetry imposed (**Fig. 5G and 5H**). Each capsid has a potential maximum
317 of 60 copies of the CVSC heteropentamer as there are 12 capsid vertices and 5 CVSC per vertex,
318 including the portal vertex [29,34-36,38,45,48-50]. For the 317 capsids in the present study, there were
319 3,804 vertices. Frequencies ranged from 290 vertices without a CVSC to 1,198 vertices with a
320 full complement of five copies of the CVSC (**Fig. 5G**). Additionally, alternative distributions of
321 the CVSC were observed at vertices where 2 or 3 copies of the heteropentamer were not adjacent
322 to one another, indicating a non-cooperative attachment of the heteropentamer to these capsid
323 vertices (**Fig. 5H**). In contrast to purified VZV C-capsids[41], intranuclear C-capsids in infected
324 cells had almost complete vertex occupancy (52; SEM = 0.861), demonstrating their maturity (**Fig.
325 5I**). CAIs with limited scaffold protein had greater CVSC occupancy (39; SEM = 0.859) compared
326 to CAIs with extensive scaffold protein (32; SEM = 0.753), providing additional evidence that the
327 former represent a stage closer to DNA encapsidation while the latter are at an earlier stage in
328 nucleocapsid synthesis. Taken together, these subnanometer resolution map observations strongly
329 support the concept that CVSC occupancy can be used as an indicator for the progression of
330 herpesvirus capsid assembly *in situ* and identifies capsids with varying levels of residual scaffold
331 protein as CAIs along a continuum, having the potential for genome packaging rather than failed
332 assembly dead ends.

333 **Portal vertex architecture differences between CAIs and C-capsids.**

334 In contrast to previous high-resolution single particle cryo-EM structures of biochemically purified
335 herpesvirus capsids, the portal vertex for VZV capsids could not be reconstructed in previous
336 reports [39,41]. To address this issue, we developed a new RELION pipeline to reconstruct the VZV
337 unique portal vertex, which was successfully identified for CAIs without the packaged dsDNA
338 genome, or C-capsids within a subset of cryo-FIB/ET tomograms using STA and 3D classification
339 of capsid vertices (**Fig. 6; Suppl. Fig. 14 to 16**). An initial cryo-ET map (23.6Å) for the unique
340 portal vertex revealed a density within the capsid cavity reminiscent of the herpesvirus portal
341 [34,38,48-50], and an absence of density for penton proteins compared to the 8.3Å cryo-ET map of the
342 capsid vertex (**Fig. 3 to 5; Suppl. Fig. 15A**). Further STA of the portal density generated a 22.9Å
343 cryo-ET map of the VZV portal with C12 symmetry (**Suppl. Fig. 15B**). A molecular model based
344 on an AlphaFold prediction of an individual VZV portal protein (pORF54; 769aa) and modelling
345 of 12 subunits based on the entire HSV-1 portal was placed into the 22.9Å cryo-ET map of the
346 VZV portal (**Suppl. Fig. 15C and 15D**). Additional densities in the portal cryo-ET map were

347 attributed to poor modelling by AlphaFold of amino acids 1 to 64 and 656 to 769, which were
348 disordered and removed from the model. Architectural differences between the portal vertices of
349 CAIs and C-capsids were visible when cryo-ET map reconstructions were performed based on
350 capsid type (**Fig 6; Suppl. Fig. 16**). The portal cap was absent for CAIs compared to C-capsids,
351 which was apparent when the entire capsid was reconstructed (**Suppl. Fig. 16**). The unique portal
352 structure of C-capsids was confirmed as the portal density in the capsid cavity was only present at
353 a single vertex (**Suppl. Fig. 16**). Further capsid-type specific architectural differences were
354 evident from portal vertex cryo-ET maps and fitment of the molecular models for the peripentonal
355 hexons, Ta and Tc triplexes, CVC1, ORF22 helices, and the portal (**Fig. 6B and 6C**). As expected,
356 densities for the pentonal MCP and alpha helices for the CVSC were absent and a channel for
357 dsDNA translocation was visible through the center for the CAIs capsid portal vertex cryo-ET
358 map. In contrast, the C-capsid cryo-ET map had a portal cap with densities for the CVSC, and
359 which filled the portal vertex channel (**Fig 6E and 6F**), presumably, tentacle helices and the
360 dsDNA genome terminus as previously described for HSV-1 [38]. As expected from the VZV vertex
361 focused classification analysis (**Fig. 5G to H**), occupancy of the CVSC at the non-portal vertices
362 of the CAI was incomplete whereas each vertex for the C-capsid exhibited a full complement of
363 the CVSC (**Fig. 6A and 6D; Suppl. Fig. 16**). These findings further support the CVSC as a
364 defining element and thus a marker of herpesvirus capsid assembly and maturity inside the cell
365 nucleus during replication.

366 **Discussion.**

367 The cell nucleus is a complex, crowded, dynamic environment, raising many questions about how
368 herpesvirus capsids assemble within this large organelle. This study reveals the power of cryo-ET
369 for the *in situ* investigation of herpesvirus assembly and morphogenesis at subnanometer
370 resolution, the localization of macromolecular structures inside herpesvirus infected cell nuclei,
371 and the reconstruction and segmentation of individual capsid proteins, allowing the identification
372 of capsid assembly intermediates (CAIs) in their native environment for replication. In addition,
373 the observations of procapsid precursors and architectural differences in capsid vertices revealed
374 by CVSC analysis of capsids in VZV infected cells provided new information relevant for
375 understanding the temporal nature of herpesvirus capsid assembly inside the cell nucleus.

376 Herpesviruses are thought to assemble in a similar fashion to dsDNA bacteriophages where the
377 capsomeres accumulate around a scaffold protein to generate procapsids [28,29]. Indeed, cell free
378 systems can recapitulate herpesvirus capsid assembly by expression of the MCP, TRX1, TRX2
379 and VP22a proteins [69]. VP22a is the scaffold protein expressed from UL26.5 (VZV ORF33.5)
380 whereas the protease is a cleavage product derived from UL26 (VZV ORF33), where the VP24
381 protease autocatalytically cleaves the UL26 gene product into VP24 and VP21 [70,71]. VP24 protease
382 activity triggers spherical procapsids to undergo angularization and the SCP (VP26) is thought to
383 provide additional capsid stability [33,72-74]. For VZV, the ORF33 protease is required for replication
384 and a SCP (ORF23) null virus produces predominantly spherical capsids, replicates poorly in cell
385 culture and is non-viable in human skin xenografts [75,76]. Furthermore, previous transient
386 transfection studies have shown that the scaffold protein (VP22a) is required for intranuclear
387 localization of the HSV-1 MCP (VP5)[77] whereas nuclear translocation of the VZV MCP is
388 impaired by deleting the SCP [76]. The high-resolution imaging inside the nucleus of VZV infected
389 cells in the present study revealed angular segment structures where capsomeres, formed by the
390 MCP and SCP, were associated with electron dense material presumed to be scaffold protein
391 (**Suppl. Fig. 2**). Previous characterization of HSV procapsid formation in cell free expression
392 systems noted their fragility and the production of angular segments, leading to a proposed model
393 where capsomeres and scaffold protein aggregate to form angular segments which in turn form
394 spherical procapsids [78]. In support of this, angular segment structures of VZV demonstrate that
395 herpesvirus procapsids form within the nucleus through cooperative assembly of capsomere-

396 associated scaffold protein subunits rather than directly on a spherical precursor structure that
397 recruits individual capsomeres.

398 Our study demonstrates that the acquisition of high-resolution 3D structure information derived
399 from vitrified cells is critical for differentiating between capsid types that occur during assembly.
400 Empty capsids were not apparent in the infected cell nucleus whereas previous observations with
401 traditional thin section EM of infected cell nuclei frequently identify capsid cavities devoid of
402 protein and dsDNA [30], leading to their conventional classification as A-capsids. From our 3D
403 observations, evidence of scaffold remnants inside the capsid cavity were lost when the 2D
404 sectional plane spans the entire diameter of the capsid, leading to their potential
405 mischaracterization. Furthermore, our data eliminate fixation, sectioning, and staining artefacts,
406 which could also lead to mischaracterization of A-capsids. In addition, capsid purification
407 methods can produce empty capsids as an artefact since the pressurized dsDNA genome can be
408 ejected due to the instability of the CVSC at the portal vertex [32]. In contrast, the 3D analyses of
409 capsid architecture coupled with the binding of CVSC heteropentamers to icosahedral vertices in
410 the infected cell points to the need for an amended classification. In the present study, capsids
411 with packaged dsDNA had the highest level of CVSC occupancy, consistent with previous single
412 particle cryo-EM of purified C-capsids [33,37,40,42,47] and, furthermore, assembly intermediates were
413 identifiable by correlating CVSC occupancy with levels of residual scaffold protein. Increasing
414 CVSC occupancy at the vertices and of heteropentamer copies (up to the maximum of five) was
415 associated with diminished quantities of scaffold protein in the capsid cavity. These observations
416 indicate that conventionally designated B-capsids represent a continuum of CAIs that can
417 potentially progress towards DNA encapsidation and formation of mature capsids ready for
418 nuclear egress.

419 Prior high-resolution cryo-EM studies of VZV capsids were not able to visualize the unique portal
420 vertex [39,41]. However, the present *in situ* study not only reconstructed the portal vertex for CAIs
421 and C-capsids but also demonstrated the acquisition of the VZV portal cap and packaged DNA for
422 C-capsids inside the infected cell nucleus. The dodecameric portal for VZV is composed of
423 pORF54 essential for the packaging and cleavage of the dsDNA genome[79,80]. Similar to the VZV
424 cryo-ET maps of the unique portal vertex in the present study, cryo-EM studies of purified HSV,
425 HCMV, KSHV, and EBV have described the molecular architecture of the portal vertex to have a
426 C12 to C5 symmetry mismatch of the portal and vertex constituents [34,35,38,49]. For HSV, the CVSC

427 is visible at the portal vertex and the CVC2 protein is required for dsDNA packaging [38]. The
428 CVC1 subunit sits atop the Ta and Tc triplexes. At the portal, for HSV-1, the Ta triplexes are
429 rotated 120° anticlockwise about their respective centers compared to pentonal Ta triplexes [38].
430 Thus, the triplexes and the CVC1 are at an altered angle compared to the other 11 vertices. The
431 MCP of HSV in the peripentonal hexon at position 6 has spine helices that extend into the pentonal
432 space at non-portal vertices [38]. The extension of the N-terminal helix was not visible in previous
433 VZV cryo-EM structures, and that absence can now be attributed to the loss of 'signal' due to the
434 combined STA of the portal and non-portal vertices [39,41]. Moreover, the head groups of the CVC2
435 dimer, important for dsDNA genome packaging and retention, form part of the portal cap, which
436 was not observed in previous studies of VZV, and explains the role of the CVSC in capsid
437 maturation.

438 In addition to the retention of the dsDNA genome, the CVSC has also been linked to nuclear
439 egress, a critical mechanism enabling capsids to leave the nucleus and enter the cytoplasm to
440 undergo herpesvirus morphogenesis [81,82]. It has also been proposed that the CVSC functions as a
441 selective switch to preferentially allow the dsDNA genome-filled C-capsids to leave the nucleus
442 [45,82]. Previous studies of capsid structures at subnanometer or near atomic resolution were
443 performed with capsids purified from the nuclei of infected cells or purified herpesvirus particles,
444 providing conflicting information about the quantities of the CVSC associated with capsid vertices
445 [33,36-41,47]. For VZV, precise information about the occupancy of the CVSC was inadequate, likely
446 due to the purification of these particles by ultracentrifugation and detergent-based removal of the
447 envelope and tegument from C-capsids [39,41]. Purification approaches have limitations in defining
448 the stages of acquisition of the CVSC on capsids. However, the extensive interactions among all
449 five subunits of the heteropentamer imply that the CVSC components co-assemble in the nucleus
450 and act together as a functional unit in binding the capsid vertices [33]. The present study provides
451 definitive proof that the CVSC can assemble as a heteropentamer and bind to capsids inside the
452 nuclei of VZV infected cells. Moreover, the application of STA and focused classification to the
453 capsids was further able to distinguish the CVSC occupancy at individual sites at the vertices and
454 from different capsid types, supporting the notion that capsids with variable levels of scaffold
455 protein are intermediates. Studies of HCMV support this concept, as the frequency of
456 morphologically defined A-capsids within infected cell nuclei was very low compared to B- and
457 C-capsids [31,32] and C-capsids purified from infected cell nuclei ejected their genomes leading to

458 higher quantities of apparent A-capsids compared to those seen by TEM [32]. Furthermore, the A-
459 capsids were covered with the HCMV tegument protein pp150, which is equivalent to the CVSC
460 of alphaherpesviruses and typically associated with C-capsids [32,42,83]. Thus, high-resolution
461 imaging coupled with state-of-the-art image classification approaches can now assign temporal
462 information to the dynamic herpesvirus capsid assembly process. The near complete occupancy
463 of the CVSC on C-capsids and the increased levels of the CVSC on capsids with limited scaffold
464 protein further support a selective function of the CVSC for nuclear egress, as both of these capsids
465 types are found in extracellular VZV particles.

466 This study provides direct evidence that the CVSC has a critical role in herpesvirus capsid
467 maturation within the host cell nucleus, revealing heterogeneity in CVSC occupancy during capsid
468 assembly, with the highest frequency found on dsDNA genome-filled C-capsids. This observation
469 sheds light on the unresolved question about whether A- and B-capsids are assembly dead ends,
470 instead suggesting that A-capsids represent artefacts from purification whereas those
471 conventionally grouped as B-capsids are assembly intermediates that can be further differentiated
472 based on CVSC occupancy. Our findings underscore the intricate and dynamic nature of capsid
473 assembly *in situ* during herpesvirus replication, providing new insights for the development of
474 novel therapeutic strategies targeting herpesvirus capsid maturation.

475

476 **Materials and Methods.**

477 ***Reagents, consumables, and resources.*** All reagents, consumables, and resources, including
478 supplier information where applicable, are provided in **Suppl. Table 5**.

479 ***Cells lines.*** MeWo cells (HTB-65; ATCC) were propagated in minimal essential medium
480 (Corning Cellgro) supplemented with 10% fetal bovine serum (FBS; Invitrogen), nonessential
481 amino acids (100 μM; Corning Cellgro), antibiotics (penicillin, 100 U/ml; streptomycin, 100
482 μg/ml; Invitrogen) and the antifungal agent amphotericin B (Invitrogen) at 37°C in a humidified
483 atmosphere with 5% CO_2.

484 ***Viruses.*** The VZV parental Oka strain was originally cloned into a bacterial artificial chromosome
485 (BAC) and designated pPOKA-BAC-DX [84]. Recombinant viruses pOka-TK-GFP (pOka-rTK)
486 and pOka-TK-RFP were generated in a previous study [85,86].

487 ***ECM micropatterning of SiO_2 EM grids.*** To position MeWo cells centrally within EM grid
488 squares, 300 mesh gold grids coated with a thin perforated layer of SiO_2 (Quantifoil R2/2) were
489 subjected to micropatterning following the procedure available at protocols.io
490 (https://www.protocols.io/view/micropatterning-em-grids-for-cryo-electron-tomogra-
491 rm7vz3wqrgx1/v1). Briefly, EM grids were exposed to atmospheric plasma, incubated in poly-L-
492 lysine (PLL, Sigma) and subsequent incubations with mPEGSuccinimidyl Valerate then PEG-
493 SVA (MW 5,000, Laysan Bio Inc). The coated grids were exposed to UV light according to a
494 digitally generated micropattern that covered the EM grid square using a Primo photo-
495 micropatterning system (Alveole) to selectively degrade the PEG coating to remove the
496 hydrophobic antifouling layer. An extracellular matrix (ECM) surrogate, Gelatin Oregon Green
497 488 (Invitrogen), was applied to the grids prior to cell seeding.

498 ***Vitrification of VZV Infected MeWo cells on ECM micropatterned grids.*** Cell free VZV cannot
499 be purified to high titers making direct infection of cells grown on EM grids with high MOIs
500 needed for productive infection impractical. Thus, infected cells were seeded directly onto ECM
501 micropatterned EM grids. VZV (pOKA-TK-RFP) infected MeWo cells were passaged onto
502 freshly seeded uninfected MeWo cells 24 hours prior to the day of seeding. On the day of seeding,
503 the VZV infected MeWo cells were then passaged onto uninfected MeWo cells and incubated for
504 8 hours. The infected cells were then trypsinized, centrifuged at 400RCF for 5 minutes then
505 resuspended in maintenance media to yield one cell per grid square; determined empirically on the

506 day of seeding. Infected and uninfected cell suspensions were applied to the ECM micropatterned
507 grids in 35mm glass bottomed dishes (MatTech P35G-1.5-14-C). After 2 hours incubation at 37°C
508 in a humidified atmosphere with 5% CO_2, 3 ml of maintenance media was added and incubated
509 for an additional 16 hours. Grids were removed from the maintenance media and plunge frozen
510 into liquid ethane using an EM GP2 (Leica) with humidity at 99% and a blot time of 9 seconds.

511 ***Cryo-FIB/SEM of vitrified VZV infected MeWo cells.*** An Aquilos 2 cryo-FIB/SEM microscope
512 (ThermoFisher) was used to generate lamella from VZV infected cells on micropatterned grids.
513 Prior to milling, the grids were platinum coated. Microexpansion joints of 1µm width and 4µm
514 between the milled area and the microexpansion joint were used to relieve tension on the final
515 lamellae[87]. The primary milling step was performed at 1nA and 5µm height and 15µm width with
516 two 1µm microexpansion joints milled either side at 4 µm from the lamella milling site.
517 Successive milling steps of 3µm (300pA), 1µm (100pA), 500nm (50pA), and a final polishing step
518 of 175nm (30pA) were performed to generate lamella with a target thickness of 175nm. Lamella
519 were produced for 6 to 10 cells per grid.

520 ***Cryo-ET of whole or cryo-FIB/SEM milled VZV infected MeWo cells.*** Tilt series were either
521 collected at the periphery of whole vitrified VZV infected MeWo cells on EM grids, using a 200kV
522 Talos Arctica (FEI) or at cryo-FIB/SEM generated lamella, using a 300kV Titan Krios (FEI)
523 controlled by SerialEM [88] to automate the data collection procedure using the parameters outlined
524 in **Suppl. Table 1**. To identify areas of interest for tilt series collection, medium magnification
525 (4,800-11,500x) montages were generated, and imaging sites were determined empirically by eye.
526 Due to the large size of herpesvirus capsids, a 3.44Å/pixel size was chosen to accommodate areas
527 where high frequencies of VZV capsids were present in the nucleus. A total of 399 tilt series were
528 collected from cryo-FIB/SEM milled lamella across five, 3-day sessions on 300kV Titan Krios
529 microscopes. A total of 194 tomograms were generated for VZV capsid quantification, analysis,
530 and cryo-ET map reconstructions.

531 ***Cryo-ET image processing.*** Motion correction, damage compensation, CTF estimation, and tilt
532 series generation was performed using Warp [89]. Tomogram reconstruction for visualization was
533 performed using the IMOD tomography GUI Etomo [90]. Tomogram processing and associated
534 movie files were generated using 3dmod [91]. Segmentation of tomograms was performed using
535 Dragonfly software (Version 2022.2 for [Windows]. Comet Technologies Canada Inc., Montreal,

536 Canada; software available at https://www.theobjects.com/dragonfly). Movies were generated
537 using FFmpeg (FFmpeg Developers. (2016). ffmpeg tool (Version be1d324) available from
538 http://ffmpeg.org/).

539 ***Subnanometer resolution cryo-ET map reconstruction of the VZV capsid vertex.*** To reconstruct
540 the VZV capsid vertex and 3-fold axis of symmetry a WARP-EMAN2 data processing strategy
541 was used (**Suppl. Fig. 9**). Tilt series generated by WARP were imported into EMAN2 for
542 tomogram alignment using patch tracking where handedness was checked and CTF measured.
543 The convolutional neural network was employed to select particles (box size 512; n=1,084 capsids)
544 from 194 tomograms and make sets (bin2). An initial model was generated from the sets using
545 e2spt_sgd_new.py (--res=50.0; --niter=30; --shrink=4; --sym=icos) followed by subtomogram-
546 subtilt refinement using e2spt_refine_new.py (--startres=30.0; --sym=icos; --iters=p3,t2,p,t,r,d; --
547 keep=0.95; --tophat localwiener –goldstandard). Classification with icosahedral symmetry was
548 performed on the output to remove poor quality particles that can negatively influence the
549 subtomogram averaging; e2spt_refinemulti_new.py (--nref 3; --maxres 40; --loadali3d; --skipali;
550 --sym icos; --maskalign spt_01/mask.hdf; --niter 20). Further refinement of 317 capsids produced
551 a cryo-ET map of the entire VZV capsids of 13.0Å resolution. To generate a subnanometer
552 resolution cryo-ET map for the VZV capsid vertex, symmetry expansion was performed with the
553 317 capsids using e2spt_extract.py (--postxf icos,0,0,110; --compressbits 8; --boxsz_unbin 192; -
554 -newlabel pent2; --mindist 500; --loadali2d) followed by building sets; e2spt_buildsets.py (--
555 label=pent2; --allparticles; --spliteo). An average of the extracted particles was generated from
556 the set using e2proc3d.py (--average; --averager mean.tomo; --avg_byxf). The average was then
557 refined using e2spt_refine_new.py (--startres=30.0; --sym=c5; --iters=p3,t2,p,t,r,d; --
558 keep=0.8,0.95,0.95; --tophat localwiener; --localrefine; --goldstandard) to achieve a cryo-ET map
559 of the VZV capsid vertex at 8.3Å resolution. A similar procedure was used for the 3-fold axis of
560 symmetry to achieve a cryo-ET map at 8.4Å resolution.

561 ***Segmentation of the 3-fold and 5-fold cryo-ET maps.*** The 3- and 5-fold cryo-ET maps of the
562 VZV capsid were segmented based on the 7BW6 asymmetric unit model of the VZV A-capsid [39]
563 using ChimeraX [92]. To segment the CVSC density in the 5-fold axis cryo-ET map, AlphaFold 2
564 [93] was used to model the heteropentamer based on the full-length proteins CVC1 (ORF43;
565 monomer) and CVC2 (ORF34; dimer), and 45 C-terminal amino acids (2724-2768) of VP1/2
566 (ORF22). Molecular dynamics flexible fitting was performed to fit the two head groups of the

567 CVC2 dimer into the cryo-ET map using NAMD [94]. A model of the asymmetric unit of the VZV
568 capsid vertex, including the CVSC, was refined using ISOLDE [95]. All images and movie files
569 were generated using ChimeraX. Movies were generated using FFmpeg.

570 ***Three axis orthogonal projection and uniform manifold approximation projection.*** VZV
571 capsids from the icosahedral refinement performed using EMAN2 were aligned to the symmetry
572 axis, and the icosahedral symmetry is applied to the particle using a missing wedge aware
573 averaging routine. Each particle was projected along three orthogonal axes, using only one quarter
574 of the volume closest to the center perpendicular to the corresponding axis. The resulting three
575 2D images per capsid are stacked together and flattened to a 1D array, which was used as input for
576 the UMAP. After manifold embedding, particles on the 2D UMAP space were clustered using a
577 K-means algorithm to produce the individual classes.

578 ***Reconstruction of the VZV Portal Vertex.*** To reconstruct the VZV portal vertex a WARP-IMOD-
579 EMAN2-Relion data processing strategy was used (**Suppl. Fig. 14**). Tilt series were aligned using
580 IMOD and for the final aligned stack, unbinned, CTF estimation was performed using CTFplotter
581 with the 'Find astigmatism option' checked. Tomograms for Relion were generated using
582 relion_tomo_reconstruct_tomogram and used for particle picking of capsids in EMAN2 (n=471).
583 Tomograms and particle coordinates were imported into Relion using Tomo Import. Make
584 pseudo-subtomos was used to make subtomograms (bin 4; 13.76 Å/pixel) using a box size (pixels)
585 of 360 and cropped box size (pixels) of 180. An initial model was generated using 3D initial model
586 and a mask was generated using Dynamo and Mask create. A 3D refinement was performed with
587 3D auto-refine with an initial low-pass filter of 50 Å and I3 symmetry. Particle reconstruction was
588 performed (bin2; 6.88Å/pixel) with Tomo reconstruct particle with a box size of 440 and cropped
589 box size of 220 with I3 symmetry, which was used to generate a new mask, followed by
590 reconstruction of subtomograms using Make pseudo-subtomos. A 3D refinement was performed
591 with 3D auto-refine with an initial low-pass filter of 30Å and I3 symmetry. The output was used
592 for Tomo frame alignment, particle reconstruction (bin 1; 3.44Å/pixel; box size 440 pixels; I3
593 symmetry), mask creation, reconstruction of subtomograms, and 3D refinement with an initial
594 low-pass filter of 14Å and I3 symmetry, generating a 12.1Å cryo-ET map of the VZV capsid.

595 Symmetry expansion was performed using relion_particle_symmetry_expand with --sym I3. This
596 process produces 5 rotations per vertex; redundant _rlnAngleRot values were removed to leave 12

597 unique vertices per capsid (n=5,652). Vertices beyond the boundaries of the tomograms were
598 removed (n=5,318). The Z height was adjusted to center the vertices in the center of the box using
599 relion_star_handler and --center_Z command. The output was used for particle reconstruction (bin
600 4; 13.76 Å/pixel; initial box size 120 pixels; cropped box size 60 pixels; C5 symmetry), mask
601 creation, reconstruction of subtomograms, and 3D refinement with an initial low-pass filter of 50Å
602 and C5 symmetry. The output was used for particle reconstruction (bin 2; 6.88 Å/pixel; box size
603 240 pixels; cropped box size 120 pixels; C5 symmetry), mask creation, reconstruction of
604 subtomograms, and 3D refinement with an initial low-pass filter of 30Å and C5 symmetry. The
605 output was used for particle reconstruction (bin 1; 3.44Å/pixel; box size 240 pixels; C5 symmetry),
606 mask creation, reconstruction of subtomograms, and 3D refinement with an initial low-pass filter
607 of 15Å and C5 symmetry, generating a 10.3Å cryo-ET map of the VZV capsid vertex.

608 The output was used to generate a cryo-ET capsid vertex map at bin 4 using the above processing
609 scheme then used to perform 3D classification (12 classes; 29 iterations). An initial 60 particles
610 were selected based on the presence of a portal density and the absence of the pentonal major
611 capsid protein then used to generate a cryo-ET portal vertex map at bin 4 using the above
612 processing scheme. A focused cylindrical mask was generated and used for further 3D
613 classification of the VZV capsid vertices yielding a total of 103 portal vertices. A final round of
614 template-based 3D classification yielded a total of 109 portal vertices. The output was used for
615 particle reconstruction (bin 2; 6.88Å/pixel; box size 240 pixels; cropped box size 120 pixels; C5
616 symmetry), mask creation, reconstruction of subtomograms, and 3D refinement with an initial
617 low-pass filter of 30Å and C5 symmetry, generating a 23.6Å cryo-ET map of the VZV capsid
618 portal vertex. To reconstruct the portal, particle reconstruction (bin 2; 6.88Å/pixel; box size 90
619 pixels; cropped box size 30 pixels; C12 symmetry), mask creation, reconstruction of
620 subtomograms, and 3D refinement with an initial low-pass filter of 30Å, C12 symmetry, and C1
621 symmetry relaxation was performed, generating a 22.9Å cryo-ET map of the VZV portal.

622 To identify portal vertex specific features, the 109 portal vertices were divided into CAI (n=62)
623 and C-capsids (n=47) based on morphological features; either scaffold protein (CAI) or genomic
624 DNA (C-capsids) inside the capsid cavity. Cryo-ET maps for the portal vertices from CAI (23.8Å)
625 and C-capsids (24.3Å) were generated as described above; particle reconstruction (bin 2;
626 6.88Å/pixel; box size 240 pixels; cropped box size 120 pixels; C5 symmetry), mask creation,
627 reconstruction of subtomograms, and 3D refinement with an initial low-pass filter of 30Å and C5

628 symmetry. Cryo-ET maps for the entire capsid from CAI (32.6Å) and C-capsids (33.6Å) were
629 generated by first adjusting the Z-height of the particles as previously described the performing
630 particle reconstruction (bin 2; 6.88Å/pixel; box size 512 pixels; cropped box size 256 pixels; I3
631 symmetry), mask creation, reconstruction of subtomograms, and 3D refinement with an initial
632 low-pass filter of 30Å, C5 symmetry, and C1 symmetry relaxation.

633 The resolution of all Relion generated cryo-ET maps were confirmed using Post-processing with
634 soft masks and assessed by Fourier Shell correlation curves with a cut-off at 0.143 from two
635 independent half-sets of the pseudosubtomograms.

636 ***Statistics and Reproducibility.*** All quantitative data were analyzed with two-way ANOVA to
637 determine statistical significance using Prism (GraphPad Software).

638 ***Data Availability.***

639 Data generated and/or analyzed during the current study are available in the paper or are appended
640 as supplementary data, and data that support this study are available from the authors upon request.
641 The original movie files, tilt series, and tomograms have been deposited in the Electron
642 Microscopy Public Image Archive (EMPIAR) with accession code EMPIAR-12464. The cryo-
643 ET maps have been deposited in the Electron Microscopy Data Bank (EMDB) with accession
644 codes EMD-49591 for the vertex cryo-ET map (model PDB 9NO1), EMD-49886 for the 3-fold
645 axis cryo-ET map and EMD-49465 to 49473 for cryo-ET maps of the portal vertex. All primary
646 data will be provided by the corresponding author upon request.

647 **Acknowledgments.**

648 Cryo-FIB-SEM and cryo-ET was performed at the Stanford-SLAC Cryo-EM Center and the
649 Stanford-SLAC Cryo-ET Specimen Preparation Center under the support of the National Institutes
650 of Health Common Fund's Transformative High Resolution Cryo-electron Microscopy Program
651 (U24GM139166 and U24GM129541); and the NIH Shared Instrumentation Grant
652 (S10OD021600). Research support was provided by NIH grants R01AI020459 (SLO),
653 R21AI159375 (SLO and WC), R01GM150905 (MC), AI15937502 (WC), and R21MH125285
654 (MC). Molecular graphics and analyses performed with UCSF ChimeraX, developed by the
655 Resource for Biocomputing, Visualization, and Informatics at the University of California, San

656 Francisco, with support from National Institutes of Health R01GM129325 and the Office of Cyber
657 Infrastructure and Computational Biology, National Institute of Allergy and Infectious Diseases.

658

659 **References.**

660 1. Arvin, A.M., Abendroth, A., and Howley, P.M. (2022). Varicella–Zoster Virus. In Fields
661 Virology: DNA Viruses, 7e, D.M. Knipe, B.A. Damania, and J.I. Cohen, eds. (Lippincott
662 Williams & Wilkins, a Wolters Kluwer business), pp. 0.

663 2. Damania, B., Cesarman, E., and Howley, P.M. (2022). Kaposi's Sarcoma Herpesvirus. In
664 Fields Virology: DNA Viruses, 7e, D.M. Knipe, B.A. Damania, and J.I. Cohen, eds.
665 (Lippincott Williams & Wilkins, a Wolters Kluwer business), pp. 0.

666 3. Gewurz, B.E., Longnecker, R.M., Cohen, J.I., and Howley, P.M. (2022). Epstein-Barr
667 Virus. In Fields Virology: DNA Viruses, 7e, D.M. Knipe, B.A. Damania, and J.I. Cohen,
668 eds. (Lippincott Williams & Wilkins, a Wolters Kluwer business), pp. 0.

669 4. Goodrum, F., Britt, W., Mocarski, E.S., and Howley, P.M. (2022). Cytomegalovirus. In
670 Fields Virology: DNA Viruses, 7e, D.M. Knipe, B.A. Damania, and J.I. Cohen, eds.
671 (Lippincott Williams & Wilkins, a Wolters Kluwer business), pp. 0.

672 5. Knipe, D.M., Heldwein, E.E., Mohr, I.J., Sodroski, C.N., and Howley, P.M. (2022).
673 Herpes Simplex Viruses: Mechanisms of Lytic and Latent Infection. In Fields Virology:
674 DNA Viruses, 7e, D.M. Knipe, B.A. Damania, and J.I. Cohen, eds. (Lippincott Williams
675 & Wilkins, a Wolters Kluwer business), pp. 0.

676 6. Krug, L.T., Pellett, P.E., and Howley, P.M. (2022). The Family Herpesviridae: A Brief
677 Introduction. In Fields Virology: DNA Viruses, 7e, D.M. Knipe, B.A. Damania, and J.I.
678 Cohen, eds. (Lippincott Williams & Wilkins, a Wolters Kluwer business), pp. 0.

679 7. Mori, Y., Zerr, D.M., Flamand, L., Pellett, P.E., and Howley, P.M. (2022). Human
680 Herpesviruses 6A, 6B, and 7. In Fields Virology: DNA Viruses, 7e, D.M. Knipe, B.A.
681 Damania, and J.I. Cohen, eds. (Lippincott Williams & Wilkins, a Wolters Kluwer
682 business), pp. 0.

683 8. Whitley, R.J., Johnston, C., and Howley, P.M. (2022). Herpes Simplex Viruses:
684 Pathogenesis and Clinical Insights. In Fields Virology: DNA Viruses, 7e, D.M. Knipe,
685 B.A. Damania, and J.I. Cohen, eds. (Lippincott Williams & Wilkins, a Wolters Kluwer
686 business), pp. 0.

687 9. Gilden, D.H., Mahalingham, R., Deitch, S., and Randall, C., J. (2006). Varicella Zoster
688 Virus Neuropathogenesis and Latency. In Alpha herpesviruses : molecular and cellular
689 biology, R.M. Sandri-Goldin, ed. (Caister Academic), pp. 402.

690 10. Banovic, T., Yanilla, M., Simmons, R., Robertson, I., Schroder, W.A., Raffelt, N.C.,
691 Wilson, Y.A., Hill, G.R., Hogan, P., and Nourse, C.B. (2011). Disseminated varicella
692 infection caused by varicella vaccine strain in a child with low invariant natural killer T
693 cells and diminished CD1d expression. J Infect Dis *204*, 1893-1901.
694 10.1093/infdis/jir660.

695 11. Gilden, D., Cohrs, R.J., Mahalingam, R., and Nagel, M.A. (2009). Varicella zoster virus
696 vasculopathies: diverse clinical manifestations, laboratory features, pathogenesis, and
697 treatment. Lancet Neurol *8*, 731-740. 10.1016/S1474-4422(09)70134-6.

698 12. Jean-Philippe, P., Freedman, A., Chang, M.W., Steinberg, S.P., Gershon, A.A., LaRussa,
699 P.S., and Borkowsky, W. (2007). Severe varicella caused by varicella-vaccine strain in a

child with significant T-cell dysfunction. Pediatrics *120*, e1345-1349. 10.1542/peds.2004-1681.

13. Johnson, R.W. (2007). Zoster-associated pain: what is known, who is at risk and how can it be managed? Herpes *14 Suppl 2*, 30-34.

14. Pahud, B.A., Glaser, C.A., Dekker, C.L., Arvin, A.M., and Schmid, D.S. (2011). Varicella zoster disease of the central nervous system: epidemiological, clinical, and laboratory features 10 years after the introduction of the varicella vaccine. J Infect Dis *203*, 316-323. 10.1093/infdis/jiq066.

15. Schmader, K. (2007). Herpes zoster and postherpetic neuralgia in older adults. Clin Geriatr Med *23*, 615-632, vii-viii. 10.1016/j.cger.2007.03.003.

16. Brunell, P.A., Geiser, C.F., Novelli, V., Lipton, S., and Narkewicz, S. (1987). Varicella-like illness caused by live varicella vaccine in children with acute lymphocytic leukemia. Pediatrics *79*, 922-927.

17. Marin, M., Meissner, H.C., and Seward, J.F. (2008). Varicella prevention in the United States: a review of successes and challenges. Pediatrics *122*, e744-751. 10.1542/peds.2008-0567.

18. Pickering, L.K., Baker, C.J., Freed, G.L., Gall, S.A., Grogg, S.E., Poland, G.A., Rodewald, L.E., Schaffner, W., Stinchfield, P., Tan, L., et al. (2009). Immunization programs for infants, children, adolescents, and adults: clinical practice guidelines by the Infectious Diseases Society of America. Clin Infect Dis *49*, 817-840. 10.1086/605430.

19. Han, J.Y., Hanson, D.C., and Way, S.S. (2011). Herpes zoster and meningitis due to reactivation of varicella vaccine virus in an immunocompetent child. Pediatr Infect Dis J *30*, 266-268. 10.1097/INF.0b013e3181f63cf9.

20. Krause, P.R., and Klinman, D.M. (2000). Varicella vaccination: evidence for frequent reactivation of the vaccine strain in healthy children. Nat Med *6*, 451-454. 10.1038/74715.

21. Whitley, R.J. (2008). Therapy of herpes virus infections in children. Adv Exp Med Biol *609*, 216-232. 10.1007/978-0-387-73960-1_16.

22. Whitley, R.J., Volpi, A., McKendrick, M., Wijck, A., and Oaklander, A.L. (2010). Management of herpes zoster and post-herpetic neuralgia now and in the future. J Clin Virol *48 Suppl 1*, S20-28. 10.1016/S1386-6532(10)70005-6.

23. Shiraki, K., Takemoto, M., and Daikoku, T. (2021). Emergence of varicella-zoster virus resistance to acyclovir: epidemiology, prevention, and treatment. Expert Rev Anti Infect Ther *19*, 1415-1425. 10.1080/14787210.2021.1917992.

24. Topalis, D., Gillemot, S., Snoeck, R., and Andrei, G. (2018). Thymidine kinase and protein kinase in drug-resistant herpesviruses: Heads of a Lernaean Hydra. Drug Resist Updat *37*, 1-16. 10.1016/j.drup.2018.01.003.

25. Harfouche, M., AlMukdad, S., Alareeki, A., Osman, A.M.M., Gottlieb, S., Rowley, J., Abu-Raddad, L.J., and Looker, K.J. (2024). Estimated global and regional incidence and prevalence of herpes simplex virus infections and genital ulcer disease in 2020: mathematical modelling analyses. Sex Transm Infect. 10.1136/sextrans-2024-056307.

741 26. Chaiyakunapruk, N., Lee, S.W.H., Kulchaitanaroaj, P., Rayanakorn, A., Lee, H., Looker,
742 K.J., Hutubessy, R., and Gottlieb, S.L. (2024). Estimated global and regional economic
743 burden of genital herpes simplex virus infection among 15-49 year-olds in 2016. BMC
744 Glob Public Health *2*, 42. 10.1186/s44263-024-00053-6.

745 27. Davison, A.J. (2007). Overview of classification. In Human Herpesviruses: Biology,
746 Therapy, and Immunoprophylaxis, A. Arvin, G. Campadelli-Fiume, E. Mocarski, P.S.
747 Moore, B. Roizman, R. Whitley, and K. Yamanishi, eds.

748 28. Baines, J.D. (2011). Herpes simplex virus capsid assembly and DNA packaging: a
749 present and future antiviral drug target. Trends Microbiol *19*, 606-613.
750 10.1016/j.tim.2011.09.001.

751 29. Heming, J.D., Conway, J.F., and Homa, F.L. (2017). Herpesvirus Capsid Assembly and
752 DNA Packaging. Adv Anat Embryol Cell Biol *223*, 119-142. 10.1007/978-3-319-53168-
753 7_6.

754 30. Gibson, W., and Roizman, B. (1972). Proteins specified by herpes simplex virus. 8.
755 Characterization and composition of multiple capsid forms of subtypes 1 and 2. J Virol
756 *10*, 1044-1052. 10.1128/JVI.10.5.1044-1052.1972.

757 31. Tandon, R., Mocarski, E.S., and Conway, J.F. (2015). The A, B, Cs of herpesvirus
758 capsids. Viruses *7*, 899-914. 10.3390/v7030899.

759 32. Stevens, A., Cruz-Cosme, R., Armstrong, N., Tang, Q., and Zhou, Z.H. (2024). Structure-
760 guided mutagenesis targeting interactions between pp150 tegument protein and small
761 capsid protein identify five lethal and two live-attenuated HCMV mutants. Virology *596*,
762 110115. 10.1016/j.virol.2024.110115.

763 33. Dai, X., and Zhou, Z.H. (2018). Structure of the herpes simplex virus 1 capsid with
764 associated tegument protein complexes. Science *360*. 10.1126/science.aao7298.

765 34. Gong, D., Dai, X., Jih, J., Liu, Y.T., Bi, G.Q., Sun, R., and Zhou, Z.H. (2019). DNA-
766 Packing Portal and Capsid-Associated Tegument Complexes in the Tumor Herpesvirus
767 KSHV. Cell *178*, 1329-1343 e1312. 10.1016/j.cell.2019.07.035.

768 35. Li, Z., Pang, J., Dong, L., and Yu, X. (2021). Structural basis for genome packaging,
769 retention, and ejection in human cytomegalovirus. Nat Commun *12*, 4538.
770 10.1038/s41467-021-24820-3.

771 36. Li, Z., Zhang, X., Dong, L., Pang, J., Xu, M., Zhong, Q., Zeng, M.S., and Yu, X. (2020).
772 CryoEM structure of the tegumented capsid of Epstein-Barr virus. Cell Res *30*, 873-884.
773 10.1038/s41422-020-0363-0.

774 37. Liu, W., Cui, Y., Wang, C., Li, Z., Gong, D., Dai, X., Bi, G.Q., Sun, R., and Zhou, Z.H.
775 (2020). Structures of capsid and capsid-associated tegument complex inside the Epstein-
776 Barr virus. Nat Microbiol *5*, 1285-1298. 10.1038/s41564-020-0758-1.

777 38. Liu, Y.T., Jih, J., Dai, X., Bi, G.Q., and Zhou, Z.H. (2019). Cryo-EM structures of herpes
778 simplex virus type 1 portal vertex and packaged genome. Nature *570*, 257-261.
779 10.1038/s41586-019-1248-6.

780 39. Sun, J., Liu, C., Peng, R., Zhang, F.K., Tong, Z., Liu, S., Shi, Y., Zhao, Z., Zeng, W.B.,
781 Gao, G.F., et al. (2020). Cryo-EM structure of the varicella-zoster virus A-capsid. Nat
782 Commun *11*, 4795. 10.1038/s41467-020-18537-y.

783 40. Wang, G., Zha, Z., Huang, P., Sun, H., Huang, Y., He, M., Chen, T., Lin, L., Chen, Z.,
784 Kong, Z., et al. (2022). Structures of pseudorabies virus capsids. Nat Commun *13*, 1533.
785 10.1038/s41467-022-29250-3.

786 41. Wang, W., Zheng, Q., Pan, D., Yu, H., Fu, W., Liu, J., He, M., Zhu, R., Cai, Y., Huang,
787 Y., et al. (2020). Near-atomic cryo-electron microscopy structures of varicella-zoster
788 virus capsids. Nat Microbiol *5*, 1542-1552. 10.1038/s41564-020-0785-y.

789 42. Yu, X., Jih, J., Jiang, J., and Zhou, Z.H. (2017). Atomic structure of the human
790 cytomegalovirus capsid with its securing tegument layer of pp150. Science *356*.
791 10.1126/science.aam6892.

792 43. Zhang, Y., Liu, W., Li, Z., Kumar, V., Alvarez-Cabrera, A.L., Leibovitch, E.C., Cui, Y.,
793 Mei, Y., Bi, G.Q., Jacobson, S., and Zhou, Z.H. (2019). Atomic structure of the human
794 herpesvirus 6B capsid and capsid-associated tegument complexes. Nat Commun *10*,
795 5346. 10.1038/s41467-019-13064-x.

796 44. Dai, X., Gong, D., Lim, H., Jih, J., Wu, T.T., Sun, R., and Zhou, Z.H. (2018). Structure
797 and mutagenesis reveal essential capsid protein interactions for KSHV replication. Nature
798 *553*, 521-525. 10.1038/nature25438.

799 45. Huet, A., Huffman, J.B., Conway, J.F., and Homa, F.L. (2020). Role of the Herpes
800 Simplex Virus CVSC Proteins at the Capsid Portal Vertex. J Virol *94*.
801 10.1128/JVI.01534-20.

802 46. Sae-Ueng, U., Liu, T., Catalano, C.E., Huffman, J.B., Homa, F.L., and Evilevitch, A.
803 (2014). Major capsid reinforcement by a minor protein in herpesviruses and phage.
804 Nucleic Acids Res *42*, 9096-9107. 10.1093/nar/gku634.

805 47. Wang, J., Yuan, S., Zhu, D., Tang, H., Wang, N., Chen, W., Gao, Q., Li, Y., Wang, J.,
806 Liu, H., et al. (2018). Structure of the herpes simplex virus type 2 C-capsid with capsid-
807 vertex-specific component. Nat Commun *9*, 3668. 10.1038/s41467-018-06078-4.

808 48. Li, Z., Pang, J., Gao, R., Wang, Q., Zhang, M., and Yu, X. (2023). Cryo-electron
809 microscopy structures of capsids and in situ portals of DNA-devoid capsids of human
810 cytomegalovirus. Nat Commun *14*, 2025. 10.1038/s41467-023-37779-0.

811 49. Machon, C., Fabrega-Ferrer, M., Zhou, D., Cuervo, A., Carrascosa, J.L., Stuart, D.I., and
812 Coll, M. (2019). Atomic structure of the Epstein-Barr virus portal. Nat Commun *10*,
813 3891. 10.1038/s41467-019-11706-8.

814 50. Schmid, M.F., Hecksel, C.W., Rochat, R.H., Bhella, D., Chiu, W., and Rixon, F.J.
815 (2012). A tail-like assembly at the portal vertex in intact herpes simplex type-1 virions.
816 PLoS Pathog *8*, e1002961. 10.1371/journal.ppat.1002961.

817 51. Draganova, E.B., Valentin, J., and Heldwein, E.E. (2021). The Ins and Outs of
818 Herpesviral Capsids: Divergent Structures and Assembly Mechanisms across the Three
819 Subfamilies. Viruses *13*. 10.3390/v13101913.

820 52. Diwaker, D., and Wilson, D.W. (2019). Microtubule-Dependent Trafficking of
821 Alphaherpesviruses in the Nervous System: The Ins and Outs. Viruses *11*.
822 10.3390/v11121165.

823 53. Zaichick, S.V., Bohannon, K.P., Hughes, A., Sollars, P.J., Pickard, G.E., and Smith, G.A.
824 (2013). The herpesvirus VP1/2 protein is an effector of dynein-mediated capsid transport
825 and neuroinvasion. Cell Host Microbe *13*, 193-203. 10.1016/j.chom.2013.01.009.

826 54. Jih, J., Liu, Y.T., Liu, W., and Zhou, Z.H. (2024). The incredible bulk: Human
827 cytomegalovirus tegument architectures uncovered by AI-empowered cryo-EM. Sci Adv
828 *10*, eadj1640. 10.1126/sciadv.adj1640.

829 55. Vijayakrishnan, S., McElwee, M., Loney, C., Rixon, F., and Bhella, D. (2020). In situ
830 structure of virus capsids within cell nuclei by correlative light and cryo-electron
831 tomography. Sci Rep *10*, 17596. 10.1038/s41598-020-74104-x.

832 56. Bucks, M.A., O'Regan, K.J., Murphy, M.A., Wills, J.W., and Courtney, R.J. (2007).
833 Herpes simplex virus type 1 tegument proteins VP1/2 and UL37 are associated with
834 intranuclear capsids. Virology *361*, 316-324. 10.1016/j.virol.2006.11.031.

835 57. Fan, W.H., Roberts, A.P., McElwee, M., Bhella, D., Rixon, F.J., and Lauder, R. (2015).
836 The large tegument protein pUL36 is essential for formation of the capsid vertex-specific
837 component at the capsid-tegument interface of herpes simplex virus 1. J Virol *89*, 1502-
838 1511. 10.1128/JVI.02887-14.

839 58. Schipke, J., Pohlmann, A., Diestel, R., Binz, A., Rudolph, K., Nagel, C.H., Bauerfeind,
840 R., and Sodeik, B. (2012). The C terminus of the large tegument protein pUL36 contains
841 multiple capsid binding sites that function differently during assembly and cell entry of
842 herpes simplex virus. J Virol *86*, 3682-3700. 10.1128/JVI.06432-11.

843 59. Reimer, L., and Kohl, H. (2008). Transmission electron microscopy : physics of image
844 formation, Fifth edition. Edition (Springer). 99931694985.

845 60. Schaffer, M., Pfeffer, S., Mahamid, J., Kleindiek, S., Laugks, T., Albert, S., Engel, B.D.,
846 Rummel, A., Smith, A.J., Baumeister, W., and Plitzko, J.M. (2019). A cryo-FIB lift-out
847 technique enables molecular-resolution cryo-ET within native Caenorhabditis elegans
848 tissue. Nat Methods *16*, 757-762. 10.1038/s41592-019-0497-5.

849 61. Baker, M.L., Jiang, W., Rixon, F.J., and Chiu, W. (2005). Common ancestry of
850 herpesviruses and tailed DNA bacteriophages. J Virol *79*, 14967-14970.
851 10.1128/JVI.79.23.14967-14970.2005.

852 62. Homa, F.L., Huffman, J.B., Toropova, K., Lopez, H.R., Makhov, A.M., and Conway, J.F.
853 (2013). Structure of the pseudorabies virus capsid: comparison with herpes simplex virus
854 type 1 and differential binding of essential minor proteins. J Mol Biol *425*, 3415-3428.
855 10.1016/j.jmb.2013.06.034.

856 63. DeRussy, B.M., Boland, M.T., and Tandon, R. (2016). Human Cytomegalovirus pUL93
857 Links Nucleocapsid Maturation and Nuclear Egress. J Virol *90*, 7109-7117.
858 10.1128/JVI.00728-16.

859 64. Evilevitch, A., and Sae-Ueng, U. (2022). Mechanical Capsid Maturation Facilitates the
860 Resolution of Conflicting Requirements for Herpesvirus Assembly. J Virol *96*, e0183121.
861 10.1128/JVI.01831-21.

862 65. McInnes, L., and Healy, J. (2018). UMAP: Uniform Manifold Approximation and
863 Projection for Dimension Reduction. ArXiv *abs/1802.03426*.

864 66. Chen, M., and Ludtke, S.J. (2021). Deep learning-based mixed-dimensional Gaussian
865 mixture model for characterizing variability in cryo-EM. Nat Methods *18*, 930-936.
866 10.1038/s41592-021-01220-5.

867 67. Zhong, E.D., Bepler, T., Berger, B., and Davis, J.H. (2021). CryoDRGN: reconstruction
868 of heterogeneous cryo-EM structures using neural networks. Nat Methods *18*, 176-185.
869 10.1038/s41592-020-01049-4.

870 68. Radermacher, M. (1988). Three-dimensional reconstruction of single particles from
871 random and nonrandom tilt series. J Electron Microsc Tech *9*, 359-394.
872 10.1002/jemt.1060090405.

873 69. Newcomb, W.W., Homa, F.L., Thomsen, D.R., Ye, Z., and Brown, J.C. (1994). Cell-free
874 assembly of the herpes simplex virus capsid. J Virol *68*, 6059-6063.
875 10.1128/JVI.68.9.6059-6063.1994.

876 70. Davison, M.D., Rixon, F.J., and Davison, A.J. (1992). Identification of genes encoding
877 two capsid proteins (VP24 and VP26) of herpes simplex virus type 1. J Gen Virol *73 (Pt*
878 *10)*, 2709-2713. 10.1099/0022-1317-73-10-2709.

879 71. Preston, V.G., Kennard, J., Rixon, F.J., Logan, A.J., Mansfield, R.W., and McDougall,
880 I.M. (1997). Efficient herpes simplex virus type 1 (HSV-1) capsid formation directed by
881 the varicella-zoster virus scaffolding protein requires the carboxy-terminal sequences
882 from the HSV-1 homologue. J Gen Virol *78 (Pt 7)*, 1633-1646. 10.1099/0022-1317-78-
883 7-1633.

884 72. Yuan, S., Wang, J., Zhu, D., Wang, N., Gao, Q., Chen, W., Tang, H., Wang, J., Zhang,
885 X., Liu, H., et al. (2018). Cryo-EM structure of a herpesvirus capsid at 3.1 A. Science
886 *360*. 10.1126/science.aao7283.

887 73. Zhou, Z.H., He, J., Jakana, J., Tatman, J.D., Rixon, F.J., and Chiu, W. (1995). Assembly
888 of VP26 in herpes simplex virus-1 inferred from structures of wild-type and recombinant
889 capsids. Nat Struct Biol *2*, 1026-1030. 10.1038/nsb1195-1026.

890 74. Cardone, G., Heymann, J.B., Cheng, N., Trus, B.L., and Steven, A.C. (2012). Procapsid
891 assembly, maturation, nuclear exit: dynamic steps in the production of infectious
892 herpesvirions. Adv Exp Med Biol *726*, 423-439. 10.1007/978-1-4614-0980-9_19.

893 75. Zhang, Z., Selariu, A., Warden, C., Huang, G., Huang, Y., Zaccheus, O., Cheng, T., Xia,
894 N., and Zhu, H. (2010). Genome-wide mutagenesis reveals that ORF7 is a novel VZV
895 skin-tropic factor. PLoS Pathog *6*, e1000971. 10.1371/journal.ppat.1000971.

896 76. Chaudhuri, V., Sommer, M., Rajamani, J., Zerboni, L., and Arvin, A.M. (2008).
897 Functions of Varicella-zoster virus ORF23 capsid protein in viral replication and the
898 pathogenesis of skin infection. J Virol *82*, 10231-10246. 10.1128/JVI.01890-07.

899 77. Nicholson, P., Addison, C., Cross, A.M., Kennard, J., Preston, V.G., and Rixon, F.J.
900 (1994). Localization of the herpes simplex virus type 1 major capsid protein VP5 to the
901 cell nucleus requires the abundant scaffolding protein VP22a. J Gen Virol *75 (Pt 5)*,
902 1091-1099. 10.1099/0022-1317-75-5-1091.

903 78. Newcomb, W.W., Homa, F.L., Thomsen, D.R., Booy, F.P., Trus, B.L., Steven, A.C.,
904 Spencer, J.V., and Brown, J.C. (1996). Assembly of the herpes simplex virus capsid:
905 characterization of intermediates observed during cell-free capsid formation. J Mol Biol
906 *263*, 432-446. 10.1006/jmbi.1996.0587.

907 79. Visalli, M.A., House, B.L., Selariu, A., Zhu, H., and Visalli, R.J. (2014). The varicella-
908 zoster virus portal protein is essential for cleavage and packaging of viral DNA. J Virol
909 *88*, 7973-7986. 10.1128/JVI.00376-14.

910 80. Visalli, R.J., and Howard, A.J. (2014). Non-axial view of the varicella-zoster virus portal
911 protein reveals conserved crown, wing and clip architecture. Intervirology *57*, 121-125.
912 10.1159/000360225.

913 81. Draganova, E.B., Zhang, J., Zhou, Z.H., and Heldwein, E.E. (2020). Structural basis for
914 capsid recruitment and coat formation during HSV-1 nuclear egress. Elife *9*.
915 10.7554/eLife.56627.

916 82. Yang, K., and Baines, J.D. (2011). Selection of HSV capsids for envelopment involves
917 interaction between capsid surface components pUL31, pUL17, and pUL25. Proc Natl
918 Acad Sci U S A *108*, 14276-14281. 10.1073/pnas.1108564108.

919 83. Dai, X., Yu, X., Gong, H., Jiang, X., Abenes, G., Liu, H., Shivakoti, S., Britt, W.J., Zhu,
920 H., Liu, F., and Zhou, Z.H. (2013). The smallest capsid protein mediates binding of the
921 essential tegument protein pp150 to stabilize DNA-containing capsids in human
922 cytomegalovirus. PLoS Pathog *9*, e1003525. 10.1371/journal.ppat.1003525.

923 84. Tischer, B.K., Kaufer, B.B., Sommer, M., Wussow, F., Arvin, A.M., and Osterrieder, N.
924 (2007). A self-excisable infectious bacterial artificial chromosome clone of varicella-
925 zoster virus allows analysis of the essential tegument protein encoded by ORF9. J Virol
926 *81*, 13200-13208. 10.1128/JVI.01148-07.

927 85. Yang, E., Arvin, A.M., and Oliver, S.L. (2014). The cytoplasmic domain of varicella-
928 zoster virus glycoprotein H regulates syncytia formation and skin pathogenesis. PLoS
929 Pathog *10*, e1004173. 10.1371/journal.ppat.1004173.

930 86. Oliver, S.L., Yang, E., and Arvin, A.M. (2017). Dysregulated Glycoprotein B-Mediated
931 Cell-Cell Fusion Disrupts Varicella-Zoster Virus and Host Gene Transcription during
932 Infection. J Virol *91*. 10.1128/JVI.01613-16.

933 87. Wolff, G., Limpens, R., Zheng, S., Snijder, E.J., Agard, D.A., Koster, A.J., and Barcena,
934 M. (2019). Mind the gap: Micro-expansion joints drastically decrease the bending of FIB-
935 milled cryo-lamellae. J Struct Biol *208*, 107389. 10.1016/j.jsb.2019.09.006.

936 88. Mastronarde, D.N. (2005). Automated electron microscope tomography using robust
937 prediction of specimen movements. J Struct Biol *152*, 36-51. 10.1016/j.jsb.2005.07.007.

938 89. Tegunov, D., and Cramer, P. (2019). Real-time cryo-electron microscopy data
939 preprocessing with Warp. Nat Methods *16*, 1146-1152. 10.1038/s41592-019-0580-y.

90. Mastronarde, D.N. (1997). Dual-axis tomography: an approach with alignment methods that preserve resolution. J Struct Biol *120*, 343-352. 10.1006/jsbi.1997.3919.

91. Kremer, J.R., Mastronarde, D.N., and McIntosh, J.R. (1996). Computer visualization of three-dimensional image data using IMOD. J Struct Biol *116*, 71-76. 10.1006/jsbi.1996.0013.

92. Pettersen, E.F., Goddard, T.D., Huang, C.C., Meng, E.C., Couch, G.S., Croll, T.I., Morris, J.H., and Ferrin, T.E. (2021). UCSF ChimeraX: Structure visualization for researchers, educators, and developers. Protein Sci *30*, 70-82. 10.1002/pro.3943.

93. Jumper, J., Evans, R., Pritzel, A., Green, T., Figurnov, M., Ronneberger, O., Tunyasuvunakool, K., Bates, R., Zidek, A., Potapenko, A., et al. (2021). Highly accurate protein structure prediction with AlphaFold. Nature *596*, 583-589. 10.1038/s41586-021-03819-2.

94. Phillips, J.C., Hardy, D.J., Maia, J.D.C., Stone, J.E., Ribeiro, J.V., Bernardi, R.C., Buch, R., Fiorin, G., Henin, J., Jiang, W., et al. (2020). Scalable molecular dynamics on CPU and GPU architectures with NAMD. J Chem Phys *153*, 044130. 10.1063/5.0014475.

95. Croll, T.I. (2018). ISOLDE: a physically realistic environment for model building into low-resolution electron-density maps. Acta Crystallogr D Struct Biol *74*, 519-530. 10.1107/S2059798318002425.

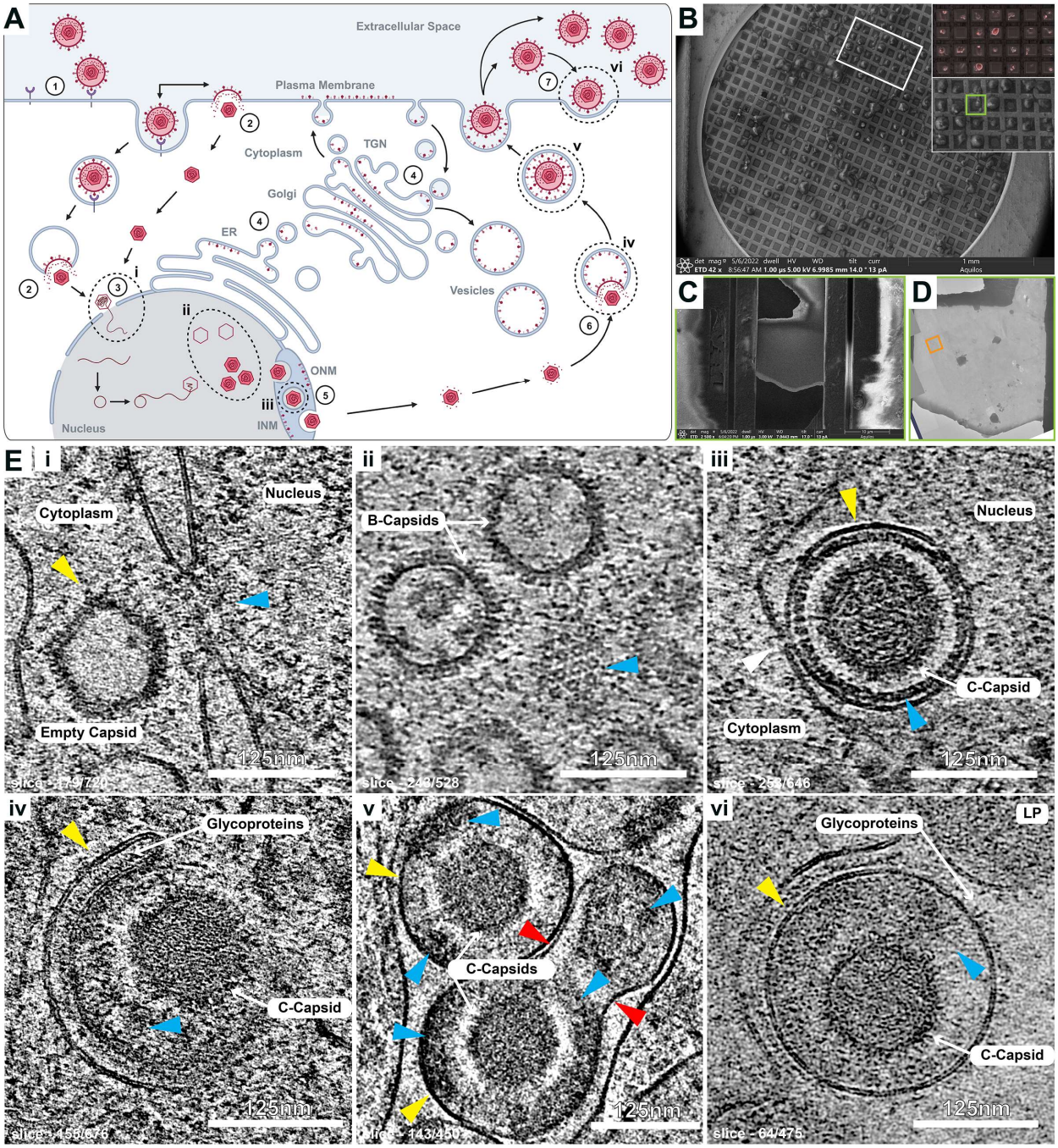

Figure 1. The VZV replication cycle and stages of morphogenesis within infected MeWo cells in 3D space captured by cryo-FIB/cryo-ET. (A) A cartoon representation (drawn using Biorender) of the VZV replication cycle where the key steps are numbered from 1 through 7 (black circles). VZV glycoproteins bind cell surface receptors during virion attachment (1), allowing the gB/gH-gL fusion complex to fuse the envelope with cell membranes either in endocytic vesicles or directly with the plasma membrane (2). The capsid is released into the cytoplasm, traffics to and docks with a nuclear pore where the dsDNA genome is injected into the cell nucleus (3) to initiate replication and capsid assembly. VZV glycoproteins necessary for attachment and cell

969 entry, are synthesized in the endoplasmic reticulum (ER) and trafficked to the Golgi during
970 maturation, exocytosed then endocytosed and trafficked to the trans-Golgi network (TGN) or
971 trafficked to the nuclear envelope (inner nuclear membrane, INM; outer nuclear membrane, ONM)
972 (4). Newly synthesized capsids undergo nuclear egress through the nuclear envelope via
973 envelopment and de-envelopment courtesy of the nuclear egress complex (5). Glycoproteins are
974 trafficked from the TGN to sites of secondary envelopment, where capsids acquire additional
975 tegument proteins, and incorporated into nascent virus particles (6). VZV particles are exported in
976 vesicular structures to the extracellular environment (7) where they can either be released into the
977 extracellular environment or attach to the plasma membrane. **(B)** Cryogenic scanning electron
978 microscopy (cryo-SEM) of VZV infected MeWo cells seeded on a micropatterned Quantifoil 300
979 mesh SiO_2 grid. The inset shows a zoomed in image of fluorescence microscopy (right top) of the
980 grid prior to vitrification (red fluorescence indicates infection with recombinant VZV expressing
981 TK-RFP) and the cryo-SEM image post vitrification (right bottom). The green square highlights
982 a single cell where a lamella was milled and presented in panels **C** and **D**. **(C)** A lamella produced
983 by cryo-FIB milling of the VZV infected cell highlighted in A. **(D)** A montage image
984 (16.85Å/pixel) produced by cryogenic transmission electron microscopy (cryo-TEM) of the
985 lamella from panel **C**. The inset orange box highlights the zoomed in area where tilt series data
986 were collected to generate a tomogram (Panel Ev; Suppl. Figure 6). **(E)** In our cryo-FIB/cryo-ET
987 data, we have captured capsids corresponding to some of the VZV replication stages labeled in
988 Roman numbers (i-vi) and outlined by dotted black ellipses in panel A. Each image is a single
989 slice through a low pass filtered tomogram. **(i)** An empty VZV capsid (yellow arrowhead) is
990 visible at the nuclear pore where the inner and outer nuclear membrane converge (blue arrowhead).
991 **(ii)** B-capsids containing scaffold protein and the capsomeres of an adjacent capsid along the 3-
992 fold axis (blue arrowhead). **(iii)** A C-capsid surrounded by the nuclear egress complex (blue
993 arrowhead) and the primary envelope (yellow arrowhead) undergoing fusion with the outer nuclear
994 membrane (white arrowhead). **(iv)** A C-capsid interacting with the tegument layer (blue
995 arrowhead) and glycoprotein-coated cell membranes (yellow arrowhead) morphing around the
996 capsid-tegument complex. **(v)** VZV particles containing C-capsids, one that has undergone
997 complete morphogenesis and a second in the process of the final steps of morphogenesis and the
998 production of a light particle. The tegument is clearly visible as the dark structures (blue
999 arrowheads) between the capsids and the VZV particle envelope (yellow arrowheads). Red
1000 arrowheads indicate a point of constriction between the formation of a complete VZV particle and
1001 a light particle. **(vi)** VZV particles released into the extracellular environment bound to the plasma
1002 membrane. One contains a C-capsid with the tegument (blue arrowheads) clearly visible as the
1003 dark structures between the capsids and the VZV particle envelope (yellow arrowheads), which is
1004 coated with glycoproteins. The second is a partially visible light particle (LP) also bound to the
1005 plasma membrane. Scale bars 125nm.
1006

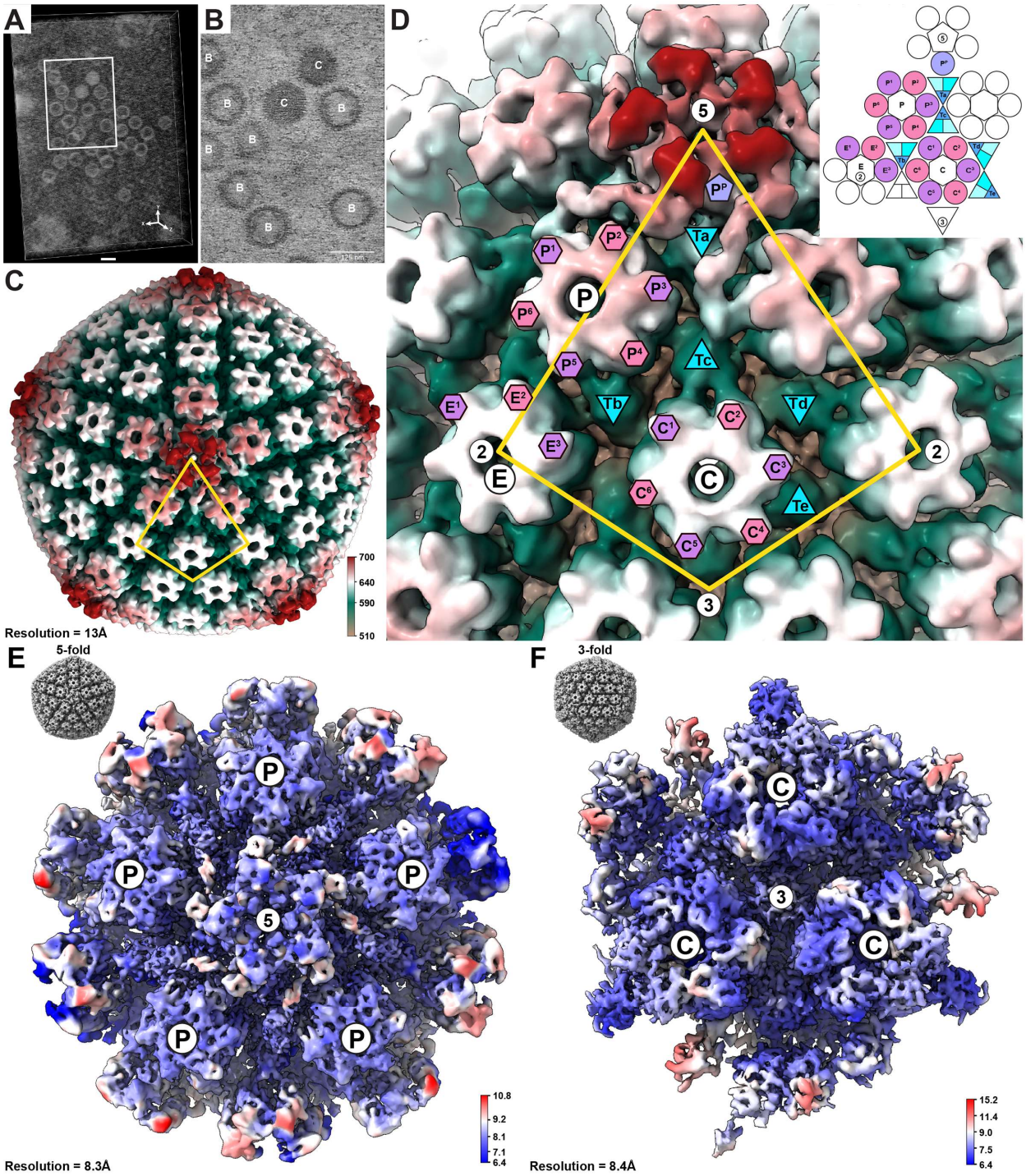

Figure 2. Cryo-ET density maps of the VZV capsid, capsid vertex, and the 3-fold symmetry axis. (A) A representative tomogram reconstruction produced from cryo-ET of a cryo-FIB/SEM milled region inside the nucleus of a vitrified, VZV infected MeWo cell represented as a 3D-volume. **(B)** A single slice from the tomogram in (**A**) in a region inside the nucleus of a vitrified VZV infected MeWo cell where a cluster of B-capsids (scaffold protein and without dsDNA labeled as B) and C-capsids (dsDNA genome labeled as C) were identified. Scale bars indicate 125nm. **(C)** Surface representation of a cryo-ET map (13Å) generated by subtomogram averaging

1015 with imposed icosahedral symmetry of 317 VZV capsids with a mixture of B and C capsids. The
1016 capsid is colored radially (510-700Å form the center of the capsid). The yellow kite connects the
1017 2-, 3-, and 5-fold axes of symmetry. **(D)** Zoom in view of a portion of (**C**) annotated with protein
1018 components that make up an asymmetric unit composed of the pentonal major capsid protein (P^P),
1019 the three types of hexon (peripentonal (P1-P6), edge (E1-E3), and center (C1-C6)), and the five
1020 triplexes (Ta, Tb, Tc, Td, and Te). The inset (right) is a schematic of the asymmetric unit of the
1021 icosahedral capsid. **(E and F)** Cryo-ET maps generated by subtomogram averaging and focused
1022 classification of the VZV capsid vertex (E; 8.3Å; EMD-49591) and 3-fold axis of symmetry (F;
1023 8.4Å; EMD-49886). The inset cryo-ET maps of the 13Å VZV capsid cryo-ET map are projected
1024 along the 5-fold (**E**) and 3-fold (**F**) axes of symmetry. Peripentonal (P) and center (C) hexons are
1025 labelled. The color key indicates the local resolution (Å) of the cryo-ET maps.
1026

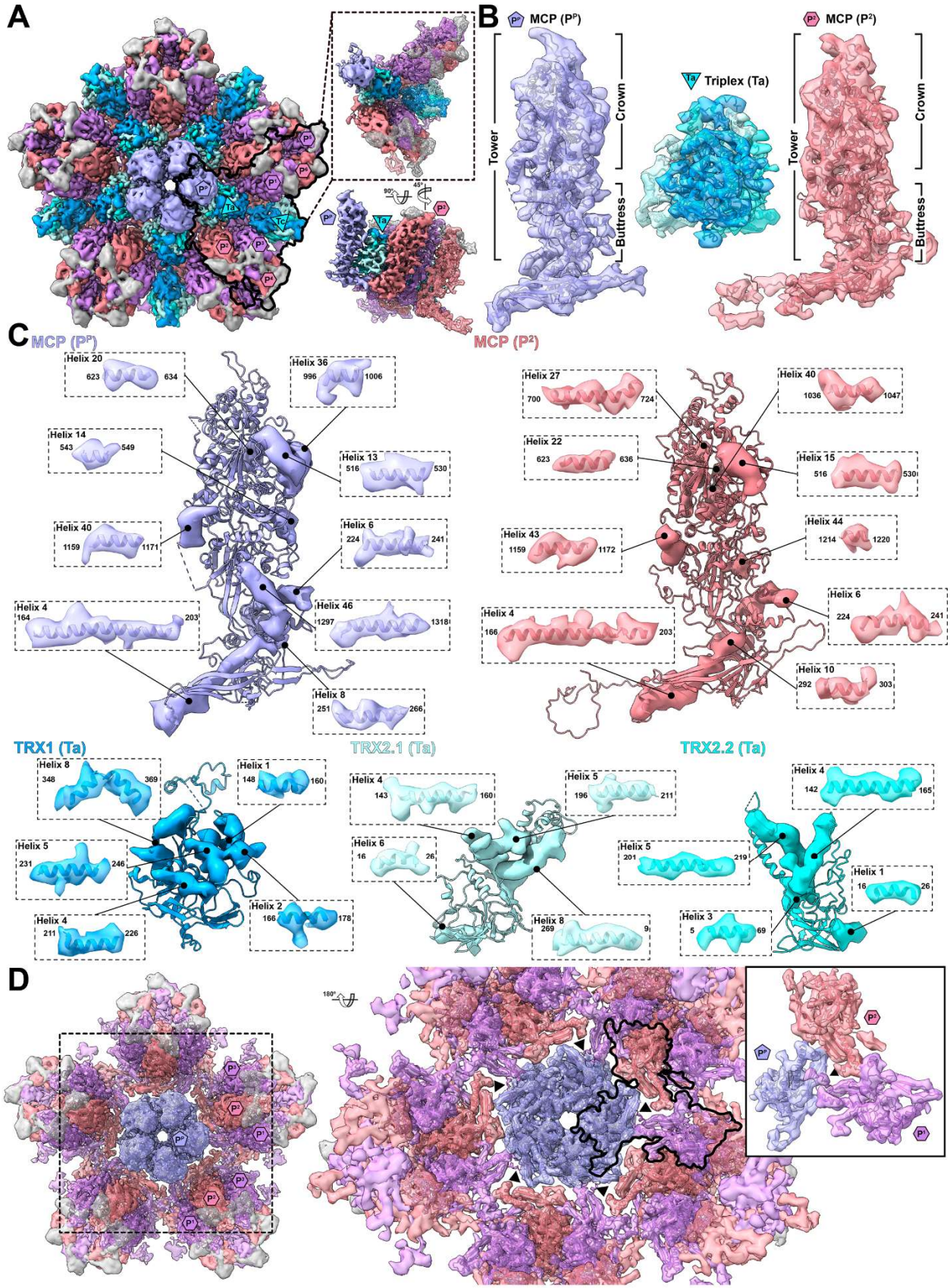
A
B
MCP (P¹)
MCP (P²)
Triplex (Ta)
Tower
Crown
Buttress
C
MCP (P¹)
MCP (P²)
Helix 20
623
634
Helix 36
996
1006
Helix 14
543
549
Helix 13
516
530
Helix 40
1159
1171
Helix 6
224
241
Helix 4
164
203
Helix 46
1297
1318
Helix 8
251
266
Helix 27
700
724
Helix 40
1036
1047
Helix 22
623
636
Helix 15
516
530
Helix 43
1159
1172
Helix 44
1214
1220
Helix 4
166
203
Helix 6
224
241
Helix 10
292
303
TRX1 (Ta)
TRX2.1 (Ta)
TRX2.2 (Ta)
Helix 8
348
369
Helix 1
148
160
Helix 5
231
246
Helix 4
211
226
Helix 2
166
178
Helix 4
143
160
Helix 5
196
211
Helix 6
16
26
Helix 8
269
Helix 4
142
165
Helix 5
201
219
Helix 1
16
26
Helix 3
5
69
D
180°

1027

1028 **Figure 3. Segmentation of the 8.3Å VZV capsid vertex cryo-ET map. (A)** Segmentation of
1029 the 8.3Å cryo-ET map based on the 7BW6[39] and a refined model based on the subnanometer map.
1030 The major capsid protein (MCP; ORF40) of the penton (P^P) and the peripentonal hexons (P^{1-6}),
1031 triplex proteins TRX1 (ORF20) and TRX2 (ORF41) for triplexes Ta and Tc, and small capsomere
1032 interacting protein (SCP; ORF23) are colored lavender blue (P^P), very soft violet ($P^{1,3,5}$), light coral
1033 ($P^{2,4,6}$), deep sky blue (TRX1), Columbia blue (TRX2.1), aqua (TRX2.2), and dark gray (SCP).
1034 The colored shapes within the black outline demarcate a pseudo-asymmetric unit (P^P, P^{1-6} and
1035 associated SCP, and triplexes Ta and Tc) of the VZV capsid vertex, which is isolated in the dotted
1036 box (inset). **(B)** Extracted densities of the P^P and P^2 MCP with the tower, buttress and crown
1037 highlighted, and Ta triplex. **(C)** Exploded views of extracted densities for helices from the P^P and
1038 P^2 MCP, and Ta triplex. Each helix is numbered according to the primary structure along with the
1039 beginning and end numbered amino acids. **(D)** Segmentation of the VZV capsid vertex without
1040 the triplexes. P^P and P^{1-3} MCPs are identified with colored shapes. The dashed boxed outlines the
1041 region shown in the right hand panel. Triangles represent the local 3-fold symmetry axes where
1042 the pentonal MCP (P^P) intersects the two peripentonal hexon MCPs, P^1 and P^2. The black outline
1043 highlights the intersection between the HK97-like fold and the P^P, P^1, and P^2 MCPs (inset).
1044

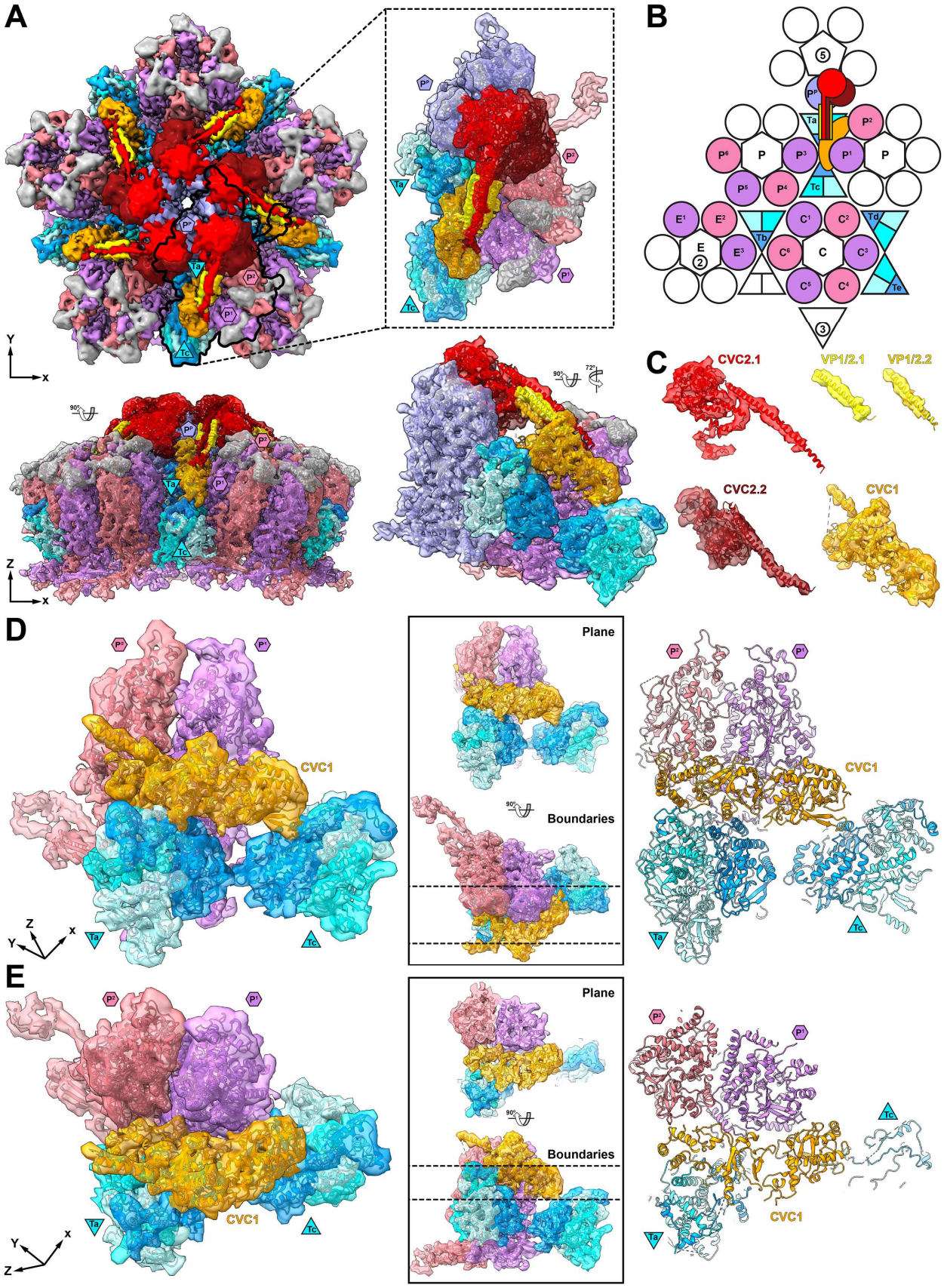
A
B
C
D
E
CVC2.1
VP1/2.1
VP1/2.2
CVC2.2
CVC1
Plane
Boundaries
Ta
Tb
Tc
Td
Te

1045

1046 **Figure 4. The VZV capsid vertex specific component redefines the asymmetric unit. (A)**
1047 Segmentation of the 8.3Å cryo-ET map of the vertex around the 5-fold axis of the capsid to isolate
1048 the CVSC and fit an AlphaFold 2 model using MDFF simulation and the 7BW6[39] model. The
1049 MCP, SCP, TRX1, and TRX2 are colored as for Fig. 3 and the CVSC subunits colored orange
1050 (CVC1; ORF43), red (CVC2.1; ORF34), falu red (CVC2.2; ORF34), yellow (VP1/2.1; ORF22),
1051 and gold (VP1/2.2; ORF22). The black outline highlights a portion of the VZV capsid vertex with
1052 the CVSC, which is isolated in the dashed box (inset). The lower panels show side views of the
1053 complete vertex map and the extracted region in the dotted box. **(B)** A cartoon representing the
1054 CVSC components' locations in relation to the redefined asymmetric unit compared to Fig 2C.
1055 Colored shapes define the pentonal major capsid protein (P^P), the three types of hexon
1056 (peripentonal (P^1-P^6), edge (E^1-E^3), and center (C^1-C^6)), the five triplexes (Ta, Tb, Tc, Td, and Te),
1057 and the CVSC. **(C)** Exploded view of the CVSC subunits. **(D and E)** Extracted densities
1058 revealing (**D**) CVC1 (ORF43) interactions with triplexes Ta and Tc, and (**E**) peripentonal hexon
1059 MCP P^1 and P^2. Models of the CVC1, TRX1, TRX2, P^1, and P^2 within the cryo-ET map densities
1060 are shown in the left-hand panels. Right hand panels show plane views of the molecular models
1061 (far right) that highlight likely interaction sites between CVC1, the triplexes (**D**), and peripentonal
1062 MCPs (**E**) and the boundaries of the planes (black boxes)
1063

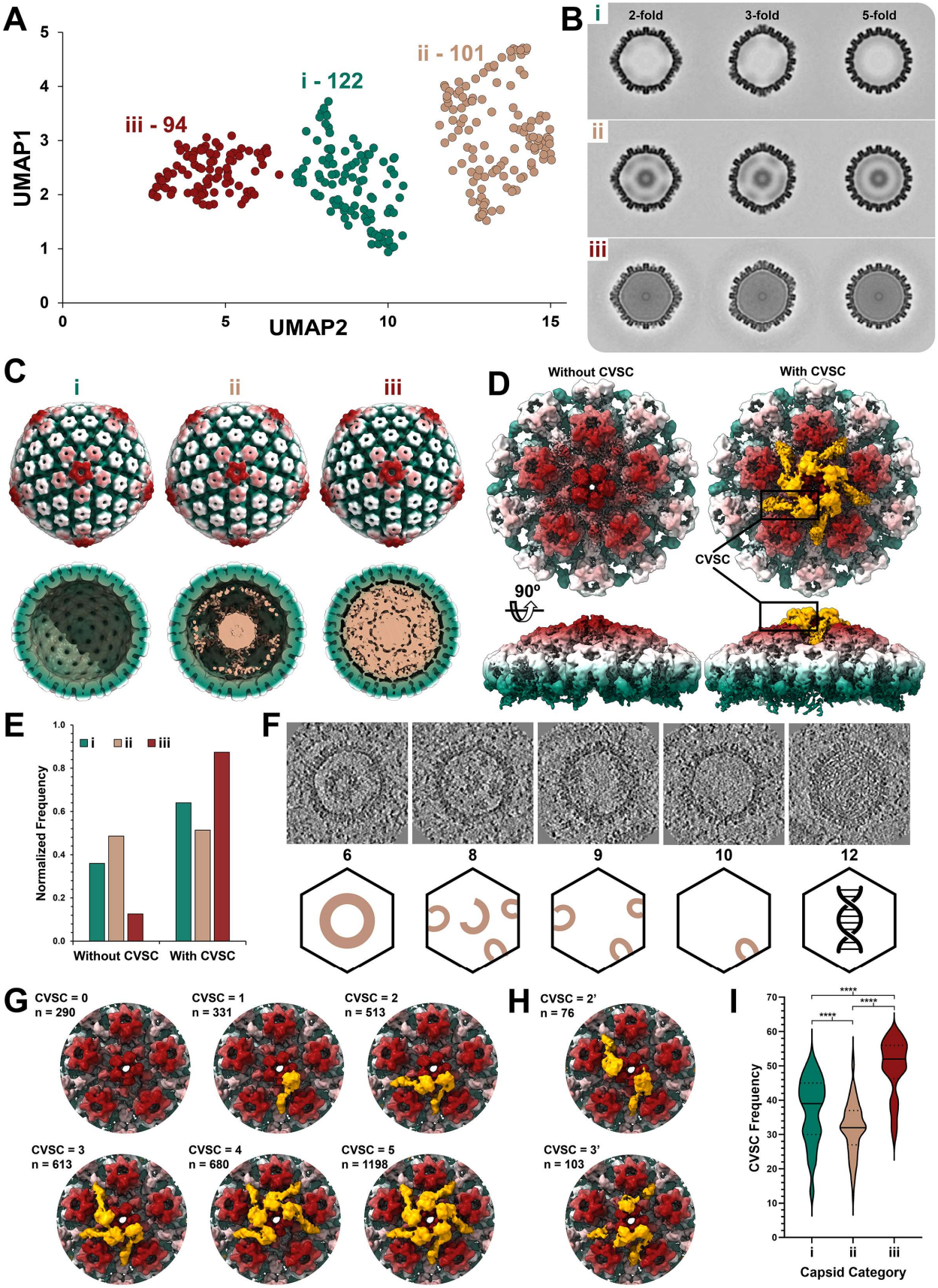
A
UMAP1
UMAP2
iii - 94
i - 122
ii - 101
B
i
ii
iii
2-fold
3-fold
5-fold
C
i
ii
iii
D
Without CVSC
With CVSC
CVSC
90º
E
i
ii
iii
Normalized Frequency
Without CVSC
With CVSC
F
6
8
9
10
12
G
CVSC = 0
n = 290
CVSC = 1
n = 331
CVSC = 2
n = 513
CVSC = 3
n = 613
CVSC = 4
n = 680
CVSC = 5
n = 1198
H
CVSC = 2'
n = 76
CVSC = 3'
n = 103
I
CVSC Frequency
Capsid Category
****

1064

1065 **Figure 5. The capsid vertex specific component as a temporal marker for herpesvirus**
1066 **capsid assembly. (A)** Uniform manifold approximation and projection (UMAP) of 317 VZV
1067 capsids producing three clusters, i, ii and iii. **(B)** 2D class averages of clusters i to iii projected
1068 along 2-, 3-, and 5-fold axes of symmetry. **(C)** Subtomogram reconstruction of the three capsid
1069 classes, i, ii, and iii. Capsids are colored radially from the center of the capsid to the outer shell;
1070 beige, green, white, and red. The transverse planes show the empty cavity, (i), scaffold filled cavity
1071 (ii), and DNA filled cavity (iii) of the VZV capsids. **(D)** Subtomogram reconstructions of the
1072 capsid vertex without and with the CVSC. The vertices are colored radially as for panel B with
1073 the CVSC colored yellow. **(E)** Normalized frequency of i, ii, and iii capsid classes without or
1074 with the CVSC. **(F)** Increased CVSC occupancy at capsid vertices associated with decreased
1075 scaffold protein. Slice view of representative polished particles (EMAN2) extracted from
1076 tomograms and cartoons depicting the scaffold protein visible in the capsid cavity. Numbers
1077 represent the frequency of vertices occupied with the CVSC. **(G)** Subtomogram averaging after
1078 symmetry relaxation and focused classification. The frequency (n) of VZV capsid vertices without
1079 (0) or with 1 to 5 copies of the CVSC (yellow) is indicated for each vertex. **(H)** Non-consecutive
1080 distribution of the CVSC (yellow) at the VZV capsid vertices with the frequency (n) of 2 (2') or 3
1081 (3') copies after subtomogram averaging and focused classification. **(I)** A violin plot representing
1082 the frequency of the CVSC (60 copies per capsid; 5 CVSC subunits per 12 vertices of the capsid)
1083 for each capsid class, i, ii and iii. The solid line represents the median and the dotted lines represent
1084 quartiles. Asterisks above the violin plots indicate p-values (<0.0001) for significant differences
1085 from a Tukey's multiple comparison test.

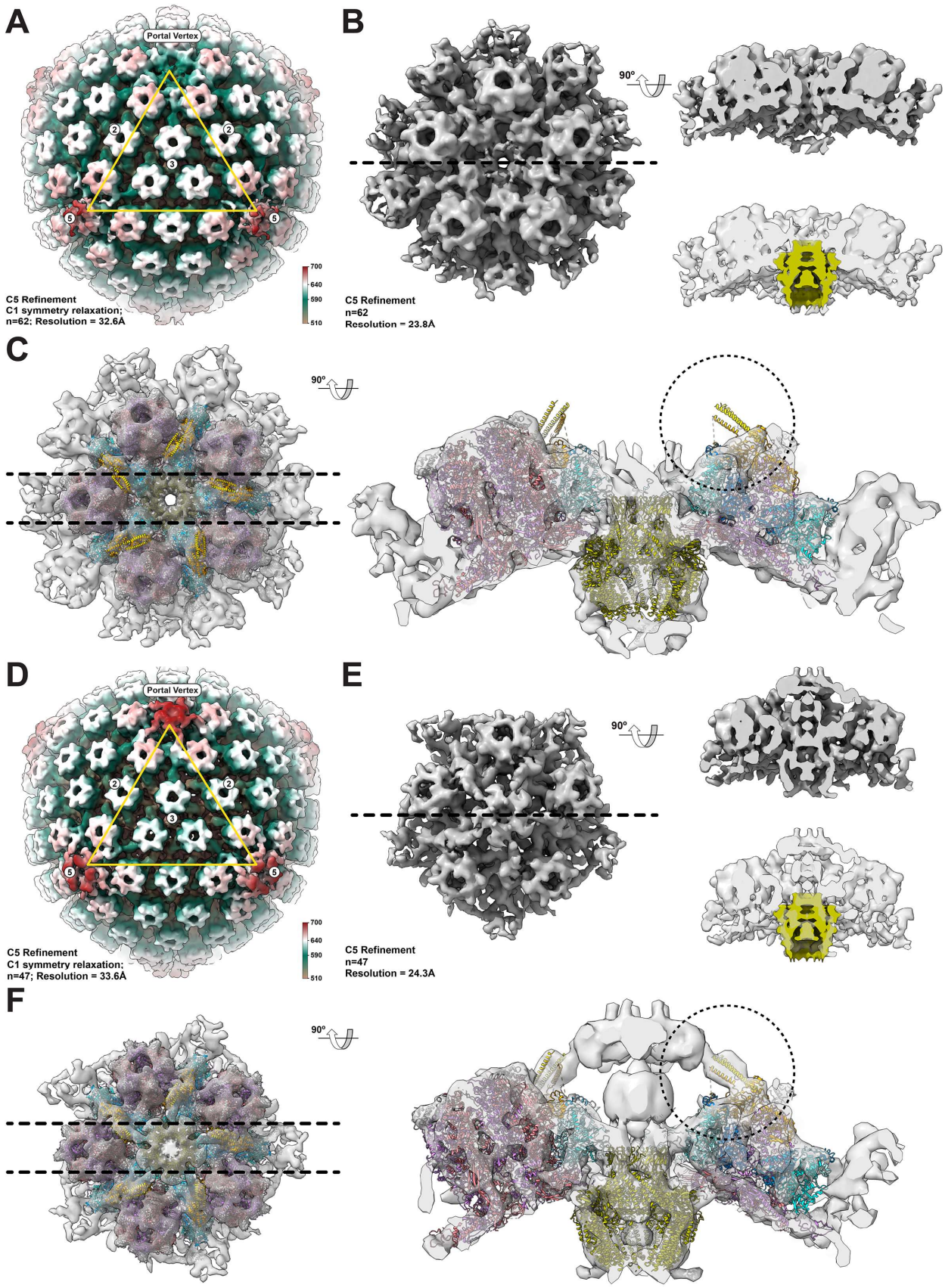
A
Portal Vertex
2
2
3
5
5
700
640
590
510
C5 Refinement
C1 symmetry relaxation;
n=62; Resolution = 32.6Å
B
90°
C5 Refinement
n=62
Resolution = 23.8Å
C
90°
D
Portal Vertex
2
2
3
5
5
700
640
590
510
C5 Refinement
C1 symmetry relaxation;
n=47; Resolution = 33.6Å
E
90°
C5 Refinement
n=47
Resolution = 24.3A
F
90°

1086

1087 **Figure 6. Differences in portal vertex architecture between VZV CAIs and C-capsids. (A**
1088 **to F)** Cryo-ET maps of CAI and C-capsids and their portal vertices. **(A and D)** Cryo-ET maps of
1089 the VZV CAIs (A; EMD-49470) and C-capsid (D; EMD-49472) projected along the 3-fold axis
1090 of symmetry and colored radially (510-700Å form the center of the capsid). The yellow triangle
1091 encompasses the 2-, 3-, and 5-fold axes of symmetry. **(B and E)** Cryo-ET maps of the portal
1092 vertices from CAIs (B; EMD-49471) and C-capsids (E; EMD-49473). The left-hand panels show
1093 the vertices along the Z-axis of the cryo-ET map. The dashed black line shows the slice for views
1094 along the Y-axis, upper right-hand panels. The lower right-hand panels for the CAIs and C-capsids
1095 show transparent views of the cryo-ET maps with the portal map (see Suppl. Fig 15) aligned to the
1096 portal vertex map density. **(C and F)** The molecular model of the VZV capsid vertex without the
1097 pentonal MCP was fit into the cryo-ET maps of the CAIs and C-capsid portal vertices. The MCP
1098 of peripentonal hexons, triplexes Ta and Tc (TRX1, TRX2.1, and TRX2.2), small capsomere
1099 interacting protein (SCP), CVSC subunits CVC1, VP1/2.1 and VP1/2.2, and the VZV portal
1100 protein ORF54 are colored light coral or very soft violet (MCP), deep sky blue (TRX1), Columbia
1101 blue (TRX2.1), aqua (TRX2.2), dark gray (SCP), orange (CVC1), yellow (VP1/2.1), gold
1102 (VP1/2.2), and olive yellow (ORF54). Dashed lines indicate the slices used for the right-hand
1103 panels to more clearly visualize the portal. The dashed circles highlight the absence of CVSC
1104 densities in the portal vertex cryo-ET map for the B-capsid compared to the C-capsid (right-hand
1105 panels).

1106

1107

1108

1109